Journal of Materials Chemistry C

ROYAL SOCIETY OF CHEMISTRY

PAPER

View Article Online
View Journal | View Issue

Cite this: J. Mater. Chem. C, 2022, 10, 4646

Photoluminescence and electrochemiluminescence of thermally activated delayed fluorescence (TADF) emitters containing diphenylphosphine chalcogenide-substituted carbazole donors†‡

Shiv Kumar,§[a] Pauline Tourneur,§[b] Jonathan R. Adsetts,§[c] Michael Y. Wong,[a] Pachaiyappan Rajamalli,[a] Dongyang Chen,[a] Roberto Lazzaroni,[bd] Pascal Viville,[d] David B. Cordes,[a] Alexandra M. Z. Slawin,[a] Yoann Olivier,*[e] Jérôme Cornil,*[b] Zhifeng Ding*[c] and Eli Zysman-Colman*[a]

Received 26th November 2021,
Accepted 7th February 2022

DOI: 10.1039/d1tc05696d

rsc.li/materials-c

Aiming to develop efficient blue-emitting thermally activated delayed fluorescence (TADF) compounds, we have designed and synthesized derivatives of the well-known sky-blue emitter **2CzPN** that contain electron-accepting phosphine chalcogenide groups to stabilize the HOMO level relative to the pristine compound, thus increasing the HOMO–LUMO gap and blue-shifting the emission wavelength. By cyclic voltammetry, photophysical data and quantum-chemical calculations, it was found that polar solvents and matrices validated the proposed concept, but these trends were not recovered in non-polar media. The suitability of these **2CzPN** derivatives in polar matrices for optoelectronic applications was explored with electrochemiluminescence (ECL) by measuring emission delays, radical stability, emission stabilities, emission efficiencies and emission spectra. Some of the **2CzPN** derivatives showed an unprecedented delayed onset of the ECL, and delayed rising time to the ECL maximum, as well as long ECL emission decay. All of these mentioned delay times suggest that these luminophores primarily emit *via* organic long-persistent electrochemiluminescence (OLECL) mechanisms. The derivatization of the donor groups of the emitters affected both the radical stability and the predominant emission mechanism, providing important insight into their potential as emitters in solid-state electroluminescent devices.

1. Introduction

Developing strategies to harvest triplet states in organic light-emitting diodes (OLEDs) based on small molecules has been the focus of considerable effort because, according to spin statistics, they constitute 75% of the excitons generated in the device.[1] While phosphorescent heavy-metal-based organometallic complexes have successfully achieved 100% internal quantum efficiency (IQE) thanks to their large spin–orbit coupling (SOC) and hence rapid intersystem crossing (ISC) rates, the use of scarce elements such as iridium and platinum is a detracting feature that will ultimately impact large-scale application of OLED technology.[2] Moreover, the inherent instability of blue-emitting heavy metal phosphorescent OLEDs has meant this class of materials is a non-starter in commercial devices.[3]

Materials showing thermally activated delayed fluorescence (TADF), which typically take the form of donor–acceptor organic compounds, have attracted tremendous recent attention as they are capable of efficiently harvesting triplet excitons.[4–8] For the TADF mechanism to be operational, there must exist a suitably

[a] Organic Semiconductor Centre, EaStCHEM School of Chemistry, University of St Andrews, St Andrews, Fife, KY16 9ST, UK. E-mail: eli.zysman-colman@st-andrews.ac.uk; Web: http://www.zysman-colman.com
[b] Laboratory for Chemistry of Novel Materials, University of Mons, Mons, Belgium. E-mail: Jerome.Cornil@umons.ac.be; Web: http://morris.umons.ac.be/
[c] Department of Chemistry, The University of Western Ontario, London, Ontario N6A 3K7, Canada. E-mail: zfding@uwo.ca; Web: https://publish.uwo.ca/~zfding/
[d] Materia Nova, Materials R&D center, Mons, Belgium. E-mail: Pascal.Viville@materianova.be; Web: http://www.materianova.be/
[e] Unité de Chimie Physique Théorique et Structurale (UCPTS) & Laboratoire de Physique du Solide (LPS), Namur Institute of Structured Matter (NISM), University of Namur, Namur, Belgium. E-mail: yoann.olivier@unamur.be

† The research data supporting this publication can be accessed at https://doi.org/10.17630/bce6c07c-64b9-4798-9a7b-8eef47d3124e.

‡ Electronic supplementary information (ESI) available: Experimental section, general synthetic procedure, photophysical measurements, electrochemical measurements, theoretical modelling, synthesis, chemical characterization, X-ray crystallography, additional electrochemical experiments and electrochemiluminescence. CCDC 2107137–2107141. For ESI and crystallographic data in CIF or other electronic format see DOI: 10.1039/d1tc05696d

§ Equally contributed.

small splitting energy (ΔE_{ST}) between the lowest excited singlet (S_1) and triplet (T_1) states. When this criterion is met, efficient reverse intersystem crossing (RISC) processes become feasible such that non-emissive triplet excitons are thermally up-converted to emissive singlet excitons.[5,9–12] In order to maintain a small ΔE_{ST}, the exchange integral between the HOMO and LUMO must be minimized,[13] and is commonly achieved by the spatial separation of these orbitals.[8,12,14] In general, there are three main molecular designs that respond to this criterion: (1) compounds with twisted conformations between donor and acceptor moieties that emit *via* an intramolecular charge-transfer state (ICT);[10] (2) compounds that promote through-space charge-transfer interactions between adjacent donor and acceptor units (TSCT);[15] and (3) compounds that are p- and/or n-doped nanographenes that emit *via* multi-resonance TADF (MR-TADF).[16] Each TADF emitter design principle has its own advantages and disadvantages in terms of emission color, color purity, photoluminescence quantum yield (Φ_{PL}), and RISC efficiency, the latter of which is correlated strongly with device stability. For example, ICT- and TSCT-based TADF emitters have both been reported to be highly emissive; their color is easily tunable but their broad emission profiles lead to poor color purity.[15,17,18] In contrast, MR-TADF emitters exhibit excellent color purity and Φ_{PL} but generally possess much lower RISC rates.[19] Regardless of emitter design, the stability of TADF OLEDs remains sub-optimal.[6]

In the pantheon of ICT emitter design, the majority of the research focus has been devoted to new acceptors while the selection of donor moieties has remained rather limited; with carbazole,[10,20,21] triphenylamine,[22–24] acridan,[25–27] phenoxazine,[28–31] phenothiazine[32,33] and dihydrophenazine[34,35] accounting for more that *ca.* 98% of all reported donors. This library of donors has been enriched through their chemical substitution that serves to tune the photophysical properties of the emitter. The majority of examples revolve around substituted carbazole derivatives and can be broadly categorized into two families: (i) substituents that enhance the electron-donating strength of carbazole and promote a red-shift in the emission, and; (ii) substituents that reduce the electron-donating strength of the carbazole and promote a blue-shift in the emission.[36] Electron-rich carbazole derivatives used within TADF emitter design include 3,6-dimethylcarbazole,[37] 3,6-dimethoxycarbazole,[38] 3,6-di-*t*-butylcarbazole,[37,38] fluorene-fused carbazole,[39] benzofuran-fused carbazole,[40] donor-dendronized carbazole[41,42] benzothiophene-fused carbazole,[43] and paracyclophane-fused carbazole.[44] In contrast, 3,6-diphenylcarbazole,[10] 9-phenylcarbazole,[45] α-/β-/δ-carboline,[46–50] indolocarbazole,[51] diphenylphosphine oxide-substituted carbazole derivatives,[52] triaryl and diarylboronate-substituted carbazole derivatives,[53] and cyanocarbazoles[54,55] represent examples of electron-poor carbazole derivatives reported in the TADF literature. In the context of blue TADF emitters employing functionalized carbazole donors, Adachi *et al.* have reported several examples of blue TADF emitters. In 2012, Adachi *et al.* reported the first example of a deep blue emitter, **DTC-DPS** (λ_{PL} = 423 nm, Φ_{PL} = 80%, ΔE_{ST} = 0.32 eV in 10 wt% in DPEPO), based on 3,6-di-(*tert*-butyl)carbazole as the donor and diphenylsulfone as the acceptor. The OLED employing this emitter showed a maximum external quantum efficiency (EQE_{max}) of 9.9% and CIE coordinates of (0.15, 0.17).[56] In a following report, an improved EQE_{max} of 14.5% and CIE coordinates of (0.16, 0.16) were reported for the emitter, **DMOC-DPS** (λ_{PL} = 455 nm, Φ_{PL} = 80%, ΔE_{ST} = 0.21 eV in 10 wt% in DPEPO) in which 3,6-di-(*tert*-butyl)carbazole (DTC) was replaced by 3,6-dimethoxycarbozole (DMOC) as the donor.[38] In another example, a sky-blue emitter **BDPCC-TRZ** (λ_{PL} = 480 nm, Φ_{PL} = 100%, ΔE_{ST} = 0.11 eV in 6 wt% in DPEPO), composed of bis(3,6-diphenylcarbazolyl)carbazole (**BDPCC**) as the donor and triphenyl-1,3,5-triazine (**TRZ**) as the acceptor, was reported. The OLED with this emitter achieved an EQE_{max} of 20.6% with λ_{EL} at 487 nm and CIE coordinates of (0.19, 0.25).[57] Lee *et al.* reported 5,11-di(9*H*-carbazol-9-yl)indolo[3,2,1-*jk*]carbazole-2-carbonitrile (**CNICCz**, λ_{PL} = 445 nm, Φ_{PL} = 46%, ΔE_{ST} = 0.27 eV) as a deep blue emitter, with a CN-modified indolocarbazole as the acceptor core and carbazole as the donor. Here, deep-blue OLEDs [λ_{EL} = 449 nm, CIE: (0.15, 0.08)] were realized with an EQE_{max} of 12.4%.[58]

In the seminal paper published in 2012, Adachi *et al.* reported one of the earliest sky-blue TADF emitters, 4,5-dicarbazolylphthalonitrile (**2CzPN**, λ_{PL} = 473 nm, Φ_{PL} = 47% in toluene).[10] An OLED device employing this emitter produced a sky-blue emission (λ_{EL} = 475 nm in 5 wt% PPT doped emitting layer) with an EQE_{max} of 8.0%. An improved OLED device performance (λ_{EL} = 483 nm, CIE: (0.17, 0.30), EQE_{max} = 13.6%) was achieved when the same emitter was used in a mCP host (λ_{PL} = 477 nm, Φ_{PL} = 89% in 6 wt% mCP doped film, ΔE_{ST} = 0.09 eV).[59] By optimizing the device architecture, Sun *et al.* were able to achieve an EQE_{max} of 21.8% [CIE: (0.17, 0.27), λ_{EL} = 480 nm] while using the same emitter in the OLED, by adopting a mixed co-host system (mCP : PO15 = 1 : 1). However, such a high EQE was only achieved at a very low current density of *ca.* 0.01 mA cm^{-2}, and the device suffered from severe efficiency roll-off at high current density.[58] In pursuit of a deeper blue color using the same general structural motif as **2CzPN**, Gyeong *et al.* reported **α-CbPN** (λ_{PL} = 445 nm, Φ_{PL} = 37%, ΔE_{ST} =0.28 eV in 20 wt% mCP doped film) and **δ-CbPN** (λ_{PL} = 480 nm, Φ_{PL} = 93%, ΔE_{ST} =0.13 eV in 20 wt% mCP doped film), employing α/δ-carboline donors in lieu of carbazole.[60] A maximum EQE of 22.5% for a sky-blue OLED with λ_{EL} = 486 nm and CIE: (0.19, 0.34) was achieved using 20 wt% **δ-CbPN** in mCP as the light-emitting layer. The same group also reported a triazine-based emitter 5,5-(2-(9*H*-carbazol-9-yl)-5-(4,6-diphenyl-1,3,5-triazin-2-yl)-1,3-phenylene)bis(5*H*-pyrido-[3,2-*b*]indole) (**CzDCbTrz**) containing a δ-carboline donor, and produced an OLED with an EQE_{max} of 23.4% and λ_{EL} = 471 nm with CIE: 0.16, 0.19 using 6 wt% emitter in 2,8-bis(diphenylphosphineoxide)-dibenzofuran (DBFPO) host. The chemical structures of blue TADF emitters discussed above are shown in Fig. 1.

Electrochemiluminescence (ECL) or electrogenerated chemiluminescence is emitted when electron transfer between electrochemically-generated radicals results in an exciton formation in the proximity of a working electrode, which relaxes radiatively.[61–64] In fact, this combination of charge recombination,

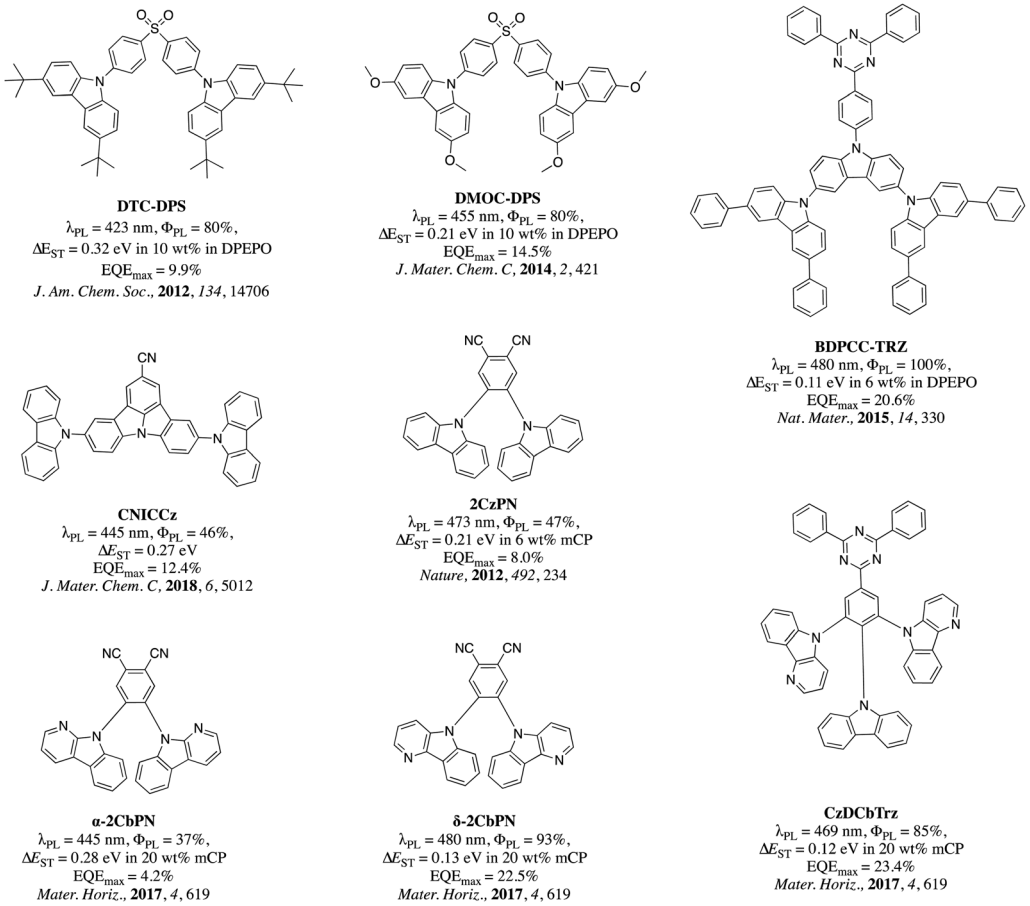

Fig. 1 Chemical structures of discussed blue TADF emitters.

radical generation, exciplex formation,[65] and possibilities of host–guest systems,[66] TADF,[67] triplet–triplet annihilation[68] and phosphorescent emissions *via* ECL mirrors photophysical processes that can occur in OLEDs. Furthermore, high luminophore concentrations, and film electrodes[61] in ECL studies can mimic bulk and interfacial molecular conditions in OLEDs, allowing predictions of molecular performance before full device manufacturing. ECL finds additional applications in discovering luminophore film enhancement phenomena,[69–71] and in commercial applications for antigen sensing.[72] Since the early studies on ECL in the 1960s,[73–75] various types of emissive compounds have been studied.[76] However, the design of commercial ECL luminophores has been mainly limited to noble-metal complexes such as those of Ru, due to their efficient and electrochemically-stable conversion of excitons to light, regardless of the total spin. Analogously to their popular use as emitters in OLEDs, TADF molecules are likewise expected to give high ECL efficiency. Despite the thousands of reports of TADF emitters used in OLEDs, there are only a small number of examples of TADF compounds employed in ECL studies. Imato *et al.* studied the annihilation ECL properties of carbazole-decorated phthalonitrile based TADF emitters in both DCM and MeCN.[67] Of the compounds investigated, the ECL emission maxima, λ_{ECL}, for **2CzPN** were modestly red-shifted (λ_{ECL} = 550 and 585 nm in DCM and MeCN, respectively) compared to the photoluminescence maxima, λ_{PL}, (λ_{PL} = 533 and 560 nm in DCM and MeCN, respectively) regardless of solvent. Further, the low Φ_{PL} (Φ_{PL} = 34 and 10% in DCM and MeCN, respectively) translated into low relative ECL efficiencies, Φ_{ECL}, of 90 and 22%, respectively, in DCM and MeCN, in comparison to $[Ru(bpy)_3]^{2+}$ which showed Φ_{ECL} = 100% under the same conditions. No discussion concerning the kinetics of exciton decay was provided. Most recently, Niu *et al.* reported the first example of a solid-state ECL study of a TADF polymer containing a backbone acridan-based donor and pendant triazine-containing acceptor, **PCzAPT10**.[77] The polymer showed significantly enhanced Φ_{ECL} of 194% relative to $[Ru(bpy)_3]^{2+}$ when using tri-*n*-propylamine (TPA) as a co-reactant, compared to the Φ_{PL} of 21%. The λ_{ECL} was also significantly red-shifted, at 587 nm, compared to the λ_{PL} (542 nm) for a neat film of **PCzAPT10** immersed in 0.1 M TBAP:MeCN electrolyte solution. Furthermore, Niu *et al.* made water-soluble **4CzIPN** nanoparticles which achieved a relative Φ_{ECL} = 0.7%, marking the first water-soluble TADF nanoparticle tested.[78]

Using the same **2CzPN** scaffold as a starting point, we hypothesized that adding strong electron-withdrawing group such as phosphine-chalcogenides onto the carbazole donor moieties would promote the desired blue-shift in the emission.

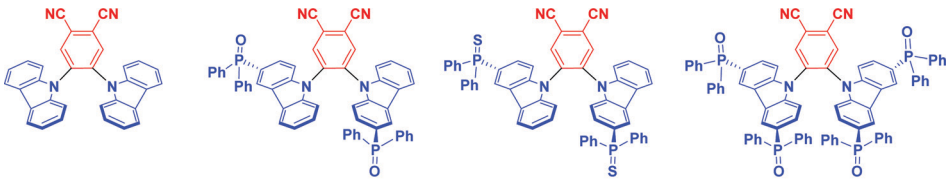

Scheme 1 Chemical structure of **2CzPN** and the three phosphine chalcogenide derivatives.

In this regard, we designed and synthesized three **2CzPN** derivatives and thoroughly investigated their physical, photophysical, electrochemical properties, further supporting these optoelectronic studies with density functional theory (DFT) calculations (Scheme 1). ECL was then used to gauge the suitability of these derivatives for optoelectronic applications in the desirable polar media. Assessing the potential of the three **2CzPN** derivatives as OLED materials was possible without the time-intensive and costly task of constructing full OLEDs, since ECL provides a tool to simulate charge imbalances, judge relative stabilities of electrically generated radical cations and anions (holes and electrons, respectively), evaluate relative emission efficiencies and understand emission mechanisms of luminophores.[67,79,80] Although our reference compound, **2CzPN** is a well-studied TADF emitter in the literature, we have redetermined its optoelectronic properties under the same conditions as the three new emitters, as well as calculating its properties, to allow the most accurate comparison.

2. Experimental section

2.1 General synthetic procedures

All commercially available chemicals and reagent grade solvents were used as received. 3-Bromocarbazole, 3,6-dibromocarbazole, *N*-TBDMS-3-bromocarbazole and *N*-TBDMS-3,6-dibromocarbazole were prepared according to the literature.[81] Air-sensitive reactions were performed using standard Schlenk techniques under a nitrogen atmosphere. Anhydrous THF was obtained from a solvent purification system. Flash column chromatography was carried out using silica gel (60 Å, 40–63 μm). Analytical thin-layer-chromatography (TLC) was performed using silica plates with aluminium backings (250 μm with F-254 indicator), and were visualized using a 254/365 nm UV lamp. ^{1}H, ^{13}C and ^{31}P NMR spectra in $CDCl_3$ or DMSO-d_6 were recorded on an NMR spectrometer (400 MHz for ^{1}H, 101 MHz for ^{13}C and 162 MHz for ^{31}P). The NMR signal is described as follows: s = singlet, d = doublet, dd = doublet of doublets, td = triplet of doublets, ddd = doublet of doublets of doublets, and m = multiplets. Melting points were measured using open-ended capillaries on Electrothermal Mel-Temp® melting point apparatus and are uncorrected. High-resolution mass spectrometry (HRMS) was performed by the EPSRC National Mass Spectrometry Service Centre (NMSSC), Swansea University. Elemental analyses were performed by Mr Stephen Boyer, London Metropolitan University. High performance liquid chromatography (HPLC) analysis was conducted on a Shimadzu Prominence Modular HPLC system. HPLC traces were performed using an ACE Excel 2 C18 analytical (3 × 150 mm) column. Gas chromatography mass spectrometry (GCMS) analysis was carried out on a Shimadzu GCMS-QP2010 SE instrument, an advanced standard gas chromatograph mass spectrometer coupled with automated AOC-5000 sample injection system using a Shimadzu-SH RTX®-1 column (fused silica) (length = 25 m, thickness = 0.25 mm, oven temp.: 40 °C to 250 °C; detector: MS; detection temp.: 250 °C; Carrier gas: helium).

Photophysical measurements. Optically dilute solutions of concentrations on the order of 10^{-5} or 10^{-6} M were prepared in HPLC grade acetonitrile for absorption and emission analyses. Absorption spectra were recorded at room temperature on a Shimadzu UV-1800 double beam spectrophotometer. The molar absorptivity values were determined by linear regression analysis of four solutions of different concentrations within the range of 10^{-4} to 10^{-5} M prepared by dilution of stock solution (10^{-3} M). Aerated solutions were prepared by using aerated solvents with prior air bubbling for 5 min whereas degassed solutions were prepared *via* five freeze–pump–thaw cycles prior to emission analysis using a home-made cuvette with extended solvent bulb designed for cryogenic degassing. Steady-state emission and time-resolved emission spectra were recorded at 298 K using Edinburgh Instruments FLS980 fluorometer. Samples were excited at 360 nm using a Xenon lamp for steady-state measurements and at 378 nm using a PicoQuant pulsed diode laser for time-resolved measurements. Photoluminescence quantum yields for solutions were determined using the optically dilute method[82] in which four sample solutions with absorbance at 360 nm being *ca.* 0.10, 0.080, 0.060 and 0.040 were used. Their emission intensities were compared with those of a reference, quinine sulfate, whose quantum yield (Φ_r) in 1 N H_2SO_4 was taken as 54.6%.[83] The photoluminescence quantum yield of a sample, Φ_s, can be determined using the equation $\Phi_s = \Phi_r(A_r/A_s)((I_s/I_r)(n_s/n_r)^2$, where A stands for the absorbance at the excitation wavelength (λ_{exc}: 360 nm), I is the integrated area under the corrected emission curve and n is the refractive index of the solvent, with the subscripts "s" and "r" representing sample and reference respectively. 10 wt% doped poly(methyl methacrylate) (PMMA)/1,3-bis(*N*-carbazolyl)benzene (mCP) thin films were prepared by spin-coating a chlorobenzene solution of the desired sample on a quartz and sapphire substrate. Solid-state Φ_{PL} measurements of thin films were performed in an integrating sphere under a nitrogen atmosphere or air using a Hamamatsu C9920-02 luminescence measurement system. For temperature-dependent measurements, samples prepared on sapphire substrates were cooled down to 77 K in a cryostat

(Oxford Instruments). Time-resolved spectra (prompt fluorescence and phosphorescence) were obtained in 10 wt% doped mCP or 10 wt% doped PMMA thin films at 77 K using a gated intensified charge coupled device (iCCD camera) from Stanford Computer Optics and under laser excitation at 360 nm.

Electrochemical measurements. All electrochemical experiments were carried out in 3 mL of DCM with a luminophore and with TBAP as the electrolyte, at concentrations of 0.7 mM and 0.1 M, respectively. A Pt electrode with an active diameter of 2 mm was used as the working electrode and was polished with 1, 0.3 and 0.05 μm aluminum oxide nanoparticles before every use. An electrochemical polish was subsequently performed in 0.1 M H_2SO_4 scanning between −0.9 and 0.9 V *vs.* Pt wire at a scan rate of 0.5 V s^{-1} for 20 minutes. The quality of the polish was verified with cyclic voltammetry of a $[Ru(bpy)_3]^{2+}$ solution at a scan rate of 0.1 V s^{-1} by seeing the 60 mV difference between the cathodic and anodic peaks for the $[Ru(bpy)_3]^{2+}$ oxidation and the same peak height. Pt coil counter and reference electrodes were used for all measurements, and calibration of the potential was performed with ferrocene as a reference. All ECL cells were constructed in an inert atmosphere glove box and were sealed to prevent oxygen from entering the cell during experiments.

ECL was measured by a photomultiplier tube (R928 PMT, Hamamatsu Photonics, Japan) held at −750 V. The voltage signal from the PMT was transduced by a Keithley ammeter (6487, Keithley Instruments, Cleveland, OH) into so-called photocurrent measured in nanoamperes (nA).

The spectroscopic measurement methods were reported elsewhere,[84] with a spectrograph (Acton 2300i, Princeton Instruments Inc., Trenton NJ) coupled with a CCD camera (Model DV420-BV, Andor Technology, UK) cooled to −55 °C.

The relative efficiency of the ECL emission was determined by finding the charge input and the ECL output for the specific experimental setup and comparing these values to the commercial standard of ECL emitter systems, $[Ru(bpy)_3]^{2+}$ for annihilation systems and $[Ru(bpy)_3]^{2+}$/BPO or $[Ru(bpy)_3]^{2+}$/TPrA for co-reactant systems, by the following equation:

$$\Phi_{ECL} = \frac{\left(\frac{\int ECL\ dt}{\int Current\ dt}\right)_x}{\left(\frac{\int ECL\ dt}{\int Current\ dt}\right)_{st}} \times 100\% \qquad (1)$$

where *st* and *x* refer to the standard $[Ru(bpy)_3]^{2+}$ and compounds of interest, respectively. Pulsing annihilation efficiencies were measured from 25 pulses using eqn (1).

Reaction enthalpies were calculated by the following equation:[85]

$$-\Delta H^\circ \le E^\circ\left(\frac{R^{\cdot+\prime}}{R'}\right) - E^\circ\left(\frac{R}{R^{\cdot-}}\right) - T\Delta S^\circ \qquad (2)$$

where E° values are the standard reduction potentials for two half reactions and $T\Delta S^\circ$ is equal to 0.1 eV when considering the temperature dependence on half reaction potentials. This measurement has an uncertainty of 0.1 eV.

3. Results and discussion

3.1 Synthesis and characterization

The synthesis of the phosphine chalcogenide-modified **2CzPN** emitters is shown in Scheme 2. Nitrogen-protected precursors 9-(*tert*-butyldimethylsilyl)-3-bromo-9*H*-carbazole, **TBDMS-BrCz** and 9-(*tert*-butyldimethylsilyl)-3,6-dibromo-9*H*-carbazole, **TBDMS-DBrCz** were prepared from their respective bromo- or dibromo-9*H*-carbazole derivatives.[81] The key intermediates, the phosphine chalcogenide-substituted carbazoles (**PPOCz**, **PPSCz**, **DiPPOCz**), were prepared by lithiation of **TBDMS-BrCz** and **TBDMS-DBrCz** followed by diphenylphosphination (**TBDMS-PPCz** and **TBDMS-DiPPCz**), and finally oxidation/sulfuration. Removal of the TBDMS group afforded the desired phosphine chalcogenide-substituted carbazole derivatives in moderate-to-excellent yield (40–95%). The respective emitters **PPOCzPN**, **PPSCzPN** and **DiPPOCzPN** were likewise obtained in moderate-to-excellent yield (52–96%) through a nucleophilic aromatic substitution reaction of 4,5-difluorophthalonitrile with **PPOCz**, **PPSCz** or **DiPPOCz**. All the emitters were characterized by ^1H, ^{13}C, and ^{31}P NMR spectroscopy and high-resolution mass spectrometry (HRMS), and their purity was demonstrated by HPLC and elemental analysis. The emitters **PPOCzPN** and **PPSCzPN** were each found to exist as a mixture of rotamers at room temperature in a ratio of 58 : 42 and 70 : 30, respectively, which was observed by both HPLC and $^{31}P\{^1H\}$ NMR spectroscopy (Fig. S1, ESI‡). This was further substantiated by obtaining single crystals of both rotamers for **PPSCzPN**.

Single crystal X-ray diffraction. The molecular structures of **PPOCzPN**, **PPSCzPN**, and **DiPPOCzPN** were determined by single crystal X-ray diffraction analysis (Fig. 2). Single crystals were grown from a binary solvent system by the vapour diffusion method: chloroform/acetonitrile and DCM/hexane for **PPOCzPN**; DCM/hexane and chloroform/methanol for **PPSCzPN**; and DCM/hexane for **DiPPOCzPN**. On initial analysis of the structure of **PPOCzPN** (obtained from chloroform/acetonitrile), partial-occupancy chlorine atoms were identified on both the

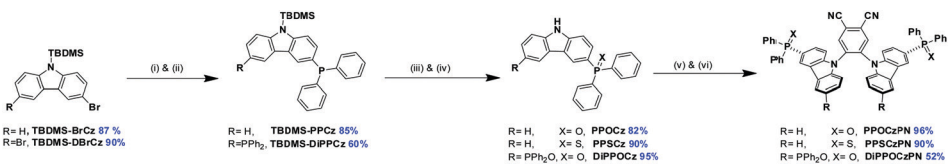

Scheme 2 Synthetic routes for the synthesis of **PPXCzPN** and **DiPPOCzPN**. Reaction conditions: (i) *n*-BuLi (1.6M), THF, −78 °C, 30 min, (ii) PPh_2Cl, −78 °C – rt, 30 min, (iii) H_2O_2 or S_8, THF, rt, 18 h, (iv) TBAF (1.0 M), THF, rt, 1 h, (v) NaH, THF, 30 min, (vi) 4,5-difluorophthalonitrile, rt, 6 h.

carbazoles, forming **PPOClCzPN**. This likely arose from chlorination during crystallization from the chloroform solvent. A later crystallisation from DCM/hexane gave rise to a structure of **PPOCzPN** not showing any chlorination. Crystallisation of **PPSCzPN** from the two different solvent combinations gave rise to crystals showing substantially different unit cells. Analysis of these revealed the presence of a different rotamer in each structure, with form **2** also showing included solvent. Only a single rotamer could be crystallised for **PPOCzPN**. In all the emitters, the interplanar angles between the donor carbazole derivatives and phthalonitrile moiety ranged between 50.71° and 59.91° and were mostly close to identical within an individual molecule [**PPOCzPN** 58.12(6)° and 59.36(6)°, **PPSCzPN-1** 50.7(3)° and 50.9(3)°, **PPSCzPN-2** 52.8(8)° and 53.9(8)°, and 51.5(7)° and 59.7(7)°, and **DiPPOCzPN** 56.82(8)° and 57.69(8)]. By contrast, a larger interplanar angle range is computed in the optimized ground-state geometries of the isolated emitters with all compounds showing one torsion angle around 45° and the other around 70° (see Section 2.3).

The four structures show a number of intermolecular interactions. In both **PPOCzPN** and **DiPPOCzPN** a three-dimensional network of weak C–H···O and C–H···N hydrogen bonded molecules is formed [**PPOCzPN** H···A distances 2.39–2.60 Å, C···A separations 3.120(2)–3.529(3) Å; **DiPPOCzPN** H···A distances 2.26–2.54 Å, C···A separations 3.018(3)–3.383(3) Å] (where *A* is the acceptor atom). The networks are reinforced by C–H···π interactions in both structures [**PPOCzPN** H···centroid distances 2.79–2.90 Å, C···centroid separations 3.549(3)–3.719(2) Å; **DiPPOCzPN** H···centroid distances 2.74 Å, C···centroid separations 3.546(3) Å], π–π interactions in **PPOCzPN** [centroid···centroid distances 3.7287(9) Å], and by conventional hydrogen bonds to the water solvent molecule in **DiPPOCzPN** [H···O distances 1.83(3) and 1.87(4) Å, O···O separations 2.811(3) and 2.858(4) Å].

Both **PPSCzPN** structures show a different pattern of interactions where weak interactions of specific types give rise to multiple one-dimensional chain structures, these being linked into two-dimensional sheets when they are combined. In **PPSCzPN-1**, C–H···π interactions [H···centroid distances 2.70 and 2.89 Å, C···centroid separations 3.623(12) and 3.799(15) Å] form chains along the *ac*-diagonal axis, and weak C–H···N hydrogen bonds [H···N distances 2.45 Å, C···N separations 3.322(16) Å] form chains along the *b*-axis. The combination of these leads to sheets in the (1 0 −1) plane. In **PPSCzPN-2**, π···π interactions [centroid···centroid distances 3.668(10)–3.803(10) Å] form chains along the *b*-axis, and C–H···π interactions [H···centroid distances 2.78 Å, C···centroid separations 3.63(3) Å] form chains along the *bc*-diagonal axis. The combination of these leads to sheets in the (1 0 0) plane, which are further reinforced by weak C–H···S hydrogen bonds [H···S distances 2.71 Å, C···S separations 3.56(2) Å]. The chloroform solvent molecules in **PPSCzPN-2** are held within the lattice by weak hydrogen bonds [H···N distances 2.54 Å, C···N separations 3.41(4) Å; H···S distances 2.62 Å, C···S separations 3.59(2) Å].

None of these structures show a matching pattern of interactions to that shown in the structure of **2CzPN**, where multiple sets of C–H···π interactions form sheets in the (0 0 1) plane, which are reinforced by weak C–H···N hydrogen bonds.[86] This is closest to what is seen in **PPSCzPN-1**, in that sheets are formed by combinations of C–H···π and C–H···N interactions; however, in **2CzPN**, the C–H···π interactions form sheets directly, whereas in **PPSCzPN-1** both the C–H···π interactions and the weak hydrogen bonds are required to form the sheets.

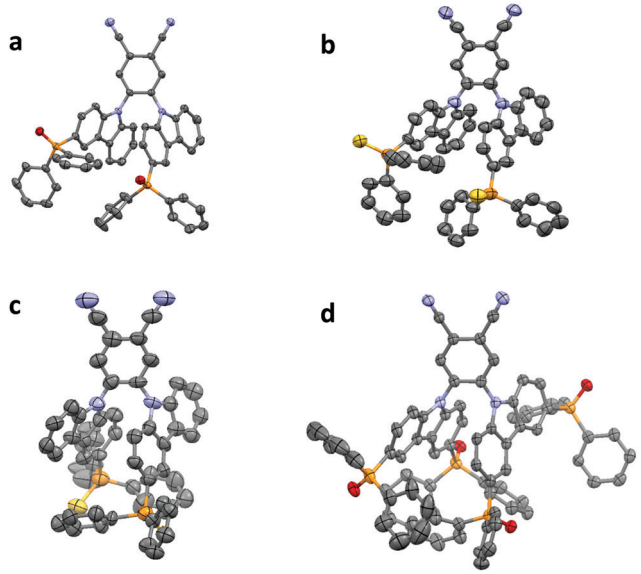

Fig. 2 Thermal ellipsoid plots of the crystal structures of (a) **PPOCzPN**, (b) **PPSCzPN-1**, (c) **PPSCzPN-2** and (d) **DiPPOCzPN**. Ellipsoids are drawn at the 50% probability level and hydrogen atoms and solvent molecules are omitted for clarity.

3.2 Electrochemical and photophysical properties

The three emitters **PPOCzPN**, **PPSCzPN** and **DiPPOCzPN** show irreversible oxidation waves and reversible reduction waves in their cyclic voltammograms (CV), recorded in DCM with 0.1 M tetrabutylammonium perchlorate (TBAP) (red curves in Fig. 3a–c). The values of the HOMO and LUMO energy levels were estimated from the peaks observed in the CV and verified from the differential pulse voltammograms (Fig. S36, ESI‡). The HOMO/LUMO levels of the reference compound **2CzPN**, as well as **PPOCzPN**, **PPSCzPN** and **DiPPOCzPN** are determined to be −6.28/−3.50, −6.39/−3.56, −6.56/−3.48 and −6.86/−3.56 eV, respectively. As expected, it is easier to reduce and harder to oxidize **DiPPOCzPN** than **PPOCzPN** due to the presence of the second electron-withdrawing diphenylphosphine oxide moiety on each carbazole. **PPOCzPN** is the easiest to oxidize and has the least stable HOMO. Similar electrochemical trends were seen in MeCN (Fig. S37, ESI‡).

The optical absorption study of **PPOCzPN**, **PPSCzPN**, **DiPPOCzPN** and the reference emitter **2CzPN** was carried out in acetonitrile (polar) and toluene (nonpolar) solvents. Table 1 summarizes the photophysical and electrochemical properties of **PPOCzPN**, **PPSCzPN**, **DiPPOCzPN** and the reference emitter **2CzPN** in polar solutions and doped films in PMMA

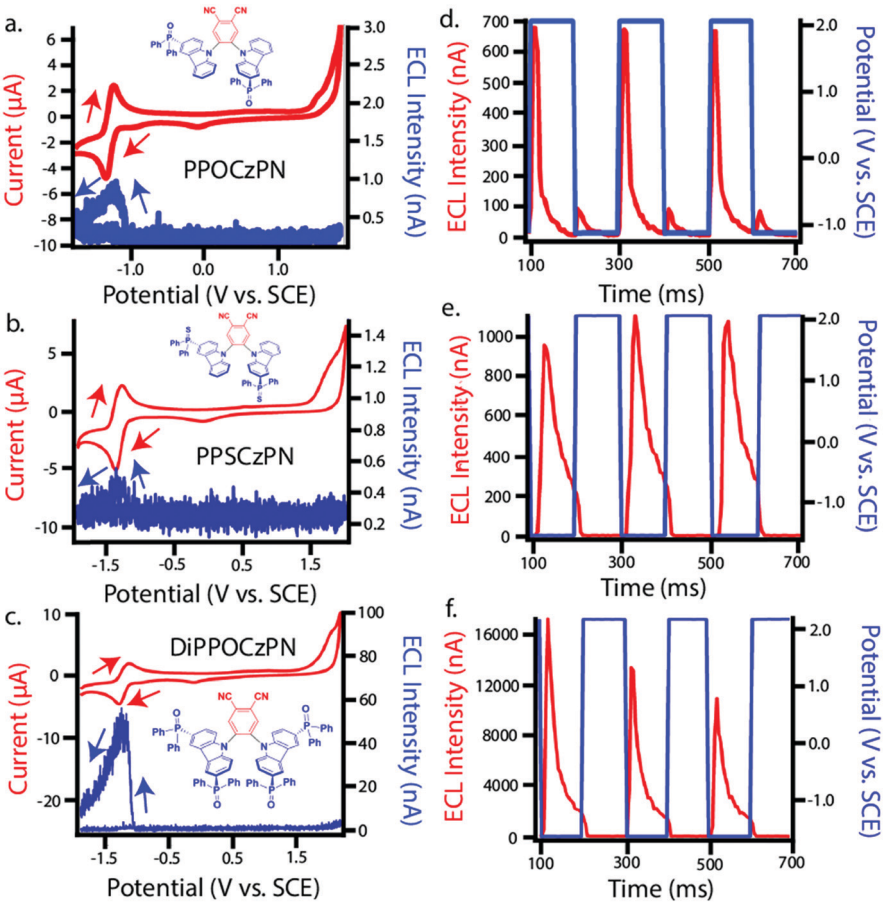

Fig. 3 (a–c) CVs (red) along with ECL–voltage curves (blue) and (d–f) ECL-time curves (red) along with voltage-time curves (blue) during potential pulsing at a pulsing frequency of 10 Hz for **PPOCzPN**, **PPSCzPN** and **DiPPOCzPN**, respectively. Scans were recorded in DCM. CVs were all performed at a scan rate of 0.1 V s^{-1} and the second cycle is shown in every case. Pulsing experiments were carried out between 0.1 V above the first oxidation and below the first reduction potentials of the compounds.

(polymethyl methacrylate) as a polar host matrix, leading to the following observations. The phosphine chalcogenide-substituted emitters exhibited similar UV-visible absorption spectra to that of **2CzPN** with three major bands observed at around 265 nm, 325 nm, and 360 nm in both solvents (Fig. 4a and d). The high-energy band near 265 nm is attributed to a LE transition of the carbazole moiety (see Fig. S40, ESI‡) while the lowest energy bands near 325 nm and 360 nm are ascribed to ICT transitions in view of their low intensity.[59] The ICT bands of the phosphine chalcogenide-substituted emitters are modestly blue-shifted by 380–1020 cm^{-1} (30–65 nm) compared to the reference emitter **2CzPN** due to the presence of the electron-withdrawing substituents. The presence of the second diphenylphosphine oxide group in **DiPPOCzPN** produced both a more intense absorption

Table 1 Summary of photophysical and electrochemical properties of **PPOCzPN**, **PPSCzPN**, **DiPPOCzPN** and **2CzPN** in polar media and in a PMMA matrix

	MeCN	DCM		10 wt% doped PMMA film		DCM		
Emitter	λ_{abs}[a]/nm, ($\varepsilon \times 10^{-4}$ M^{-1} cm^{-1})	λ_{PL}[b]/nm	Φ_{PL}[c]/%	λ_{PL}[d]/nm	Φ_{PL}[e]/%	E_{ox}/V (HOMO[f]/eV)	E_{red}/V (LUMO[f]/eV)	ΔE^g/eV
PPOCzPN	356 (1.24)	498	51	465	56	1.59 (−5.99)	−1.24 (−3.16)	2.83
PPSCzPN	358 (1.49)	501	47	465	59	1.76 (−6.16)	−1.32 (−3.08)	3.08
DiPPOCzPN	351 (1.51)	465	61	428	28	2.06 (−6.46)	−1.24 (−3.16)	3.29
2CzPN	366 (1.33)	515	29	494	77	1.48 (−5.88)	−1.30 (−3.10)	2.78
2CzPN[h]	364 (1.14)	532	29	492	76	1.50 (−5.90)[i]	−1.42 (−3.00)[i]	2.90[i]

[a] ICT band measured in MeCN at 298 K. [b] In degassed DCM (λ_{exc} = 358 nm). [c] Solution Φ_{PL} values were determined by the relative method[4] using 0.5 M quinine sulfate in H_2SO_4 (aq) as the reference (Φ_{PL}: 54.6%).[87] [d] 10 wt% doped PMMA thin films (λ_{exc} = 360 nm). [e] Absolute Φ_{PL} values in 10 wt% doped PMMA thin films under N_2. [f] In DCM with 0.1 M [^{n}Bu$_4$N]ClO$_4$ as the supporting electrolyte and SCE as the reference unless otherwise noted.[88] The HOMO and LUMO energies were calculated using the relation $E_{HOMO}/E_{LUMO} = -(E^{ox}/E^{red}$ *vs.* Fc/Fc$^+$ + 4.8) eV, where the E^{ox} and E^{red} are anodic and cathodic formal potentials, respectively, obtained from CV.[89] [g] $\Delta E = |E_{HOMO} - E_{LUMO}|$. [h] Values from ref 77. [i] Determined in MeCN.

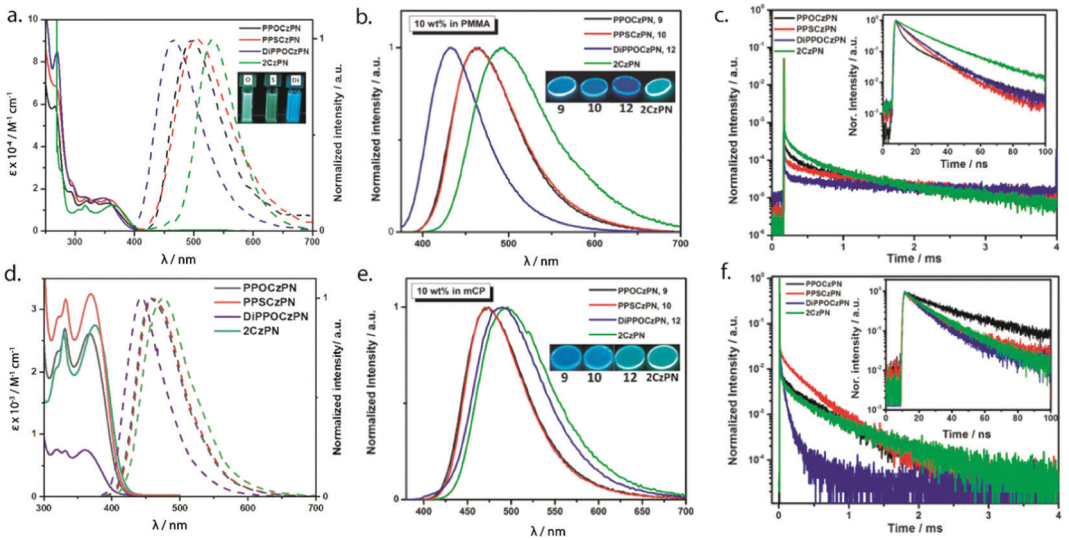

Fig. 4 (a) Absorption (solid line) and emission (dashed line) spectra of **PPOCzPN**, **PPSCzPN**, **DiPPOCzPN** and **2CzPN** recorded at room temperature in MeCN and DCM solution (λ_{exc} = 358 nm), respectively. (b) Steady-state photoluminescence spectra of 10 wt% PMMA films of **PPOCzPN**, **PPSCzPN**, **DiPPOCzPN**, **2CzPN** (λ_{exc} = 358 nm). (c) Time-resolved photoluminescence decay profiles of 10 wt% PMMA films of **PPOCzPN**, **PPSCzPN**, **DiPPOCzPN**, **2CzPN** (λ_{exc} = 378 nm). (d) Absorption and emission spectra of **PPOCzPN**, **PPSCzPN**, **DiPPOCzPN** and **2CzPN** recorded at room temperature in toluene solution (λ_{exc} = 370 nm). (e) Steady-state photoluminescence spectra of 10 wt% mCP films of **PPOCzPN**, **PPSCzPN**, **DiPPOCzPN**, **2CzPN** (λ_{exc} = 358 nm). (f) Time-resolved photoluminescence decay profiles of 10 wt% mCP films of **PPOCzPN**, **PPSCzPN**, **DiPPOCzPN**, **2CzPN** (λ_{exc} = 378 nm).

of the π–π* band at around 270 nm and the most blue-shifted ICT band. The absorption spectra did not appreciably change between toluene and acetonitrile (see Fig. 4a and d).

The photoluminescence properties of **PPOCzPN**, **PPSCzPN**, **DiPPOCzPN** and **2CzPN** were investigated in DCM and toluene, as neat films and as 10 wt% doped PMMA and mCP (1,3-bis-(*N*-carbazolyl)benzene) films, the latter matrix identified as a suitably high triplet-energy host that had previously been used with **2CzPN**. The photophysical properties are summarized in Tables 1 and 2 and the emission spectra and decay profiles of the emitters doped in PMMA and mCP thin films are shown in Fig. 4c and f. In DCM, the emission maxima shift to progressively higher energy across the series from **2CzPN** to **PPOCzPN**, **PPSCzPN**, and **DiPPOCzPN**, at 532 nm, 498 nm, 501 nm, and 465 nm, respectively, reflecting the weakening of the donor. On the other hand, owing to its lower polarity, the emission maxima of these emitters are further blue-shifted in toluene compared to DCM, a reflection of their CT character. In 10 wt% doped PMMA films, the λ_{PL} values are all blue-shifted compared to those in DCM solution at 492 nm, 465 nm, 465 nm, and 428 nm, due the less polar nature of this medium (Fig. 4b). In 10 wt% doped mCP films, the λ_{PL} values are surprisingly red-shifted and clustered closer to each other at 496 nm, 474 nm, 474 nm, and 490 nm for **2CzPN**, **PPOCzPN**, **PPSCzPN**, and **DiPPOCzPN**, respectively, in full consistency with the trends observed in toluene (Fig. 4d). The photoluminescence quantum yields, Φ_{PL}, in DCM of **PPOCzPN**, **PPSCzPN** and **DiPPOCzPN** (47–61%) are higher than that of **2CzPN** (29%).[86] The Φ_{PL} values of the emitters are somewhat lower in PMMA doped films (ranging from 28–59%), and are lower than that of **2CzPN** (76%) in the same medium. In mCP, the Φ_{PL} is recovered with values of 72%, 73% and 56% for **PPOCzPN**, **PPSCzPN** and **DiPPOCzPN**, while that of **2CzPN** is very similar to that seen in PMMA (77%). A slightly higher Φ_{PL}

Table 2 Summary of photophysical and electrochemical properties of **PPOCzPN**, **PPSCzPN**, **DiPPOCzPN** and **2CzPN** in apolar media and in the solid state in a mCP matrix and as neat films

	Toluene			10 wt% doped mCP film			Neat film	
Emitter	λ_{abs}[a]/nm	λ_{PL}[b]/nm	ΔE_{ST}[g]/eV	λ_{PL}[c]/nm	Φ_{PL}[d]/%	ΔE_{ST}[g]/eV	λ_{PL}[e]/nm	Φ_{PL}[f]/%
PPOCzPN	321, 331, 367	460	0.20	474	72	0.19	501	54
PPSCzPN	321, 332, 369	460	0.42	474	73	0.24	524	26
DiPPOCzPN	319, 332, 361	443	0.43	490	56	0.15	466	38
2CzPN	317, 329, 375	476	0.36	496	77	0.23	516	33
2CzPN	317, 329, 375[h]	484[h]	0.31[h]	477[i]	89[i]	0.09[i]	NA	NA

[a] ICT band measured in toluene at 298 K. [b] In toluene (λ_{exc} = 370 nm). [c] In 10 wt% doped mCP thin films. [d] Absolute quantum yield in 10 wt% doped mCP thin films. [e] In neat thin films. [f] Absolute quantum yield in neat thin films. [g] Measured as the energy difference between the prompt fluorescence onset (at 77 K, λ_{exc} = 378 nm, time delay = 1 ns, integration time: 1–100 ns) and the phosphorescence onset (at 77 K, λ_{exc} = 378 nm, time delay = 1 ms, integration time = 1–10 ms). [h] Values from ref. 86. [i] Values from ref. 59, measured in 6 wt% doped mCP film, ΔE_{ST} was estimated from the fluorescence (300 K) and phosphorescence (5 K) peaks. NA = not available.

(89%) has been reported for 6 wt% **2CzPN** in co-evaporated mCP thin film.[59]

Fig. 4c shows the time-resolved decay traces of the emitters in a PMMA matrix. The emission decay consisted of both prompt (τ_p) nanosecond and delayed (τ_d) microsecond fluorescence components. The prompt fluorescence decays of **PPOCzPN**, **PPSCzPN** and **DiPPOCzPN** were found to be bi-exponential with lifetimes, τ_p, ranging from 13–20 ns, similar to that of **2CzPN** (τ_p = 8, 21 ns). The delayed fluorescence decay of the three emitters is tri-exponential in nature with average lifetime of 393 μs, 416 μs, and 513 μs for **PPOCzPN**, **PPSCzPN** and **DiPPOCzPN**, respectively, significantly longer than that of **2CzPN** (τ_d = 270 μs). Fig. 4f shows the emission decays in mCP, which are similar to the decay profiles in the PMMA matrix. In this medium, the τ_p ranges from 8–37 ns, longer than those measured in PMMA, and also longer than that of **2CzPN** (τ_p = 9, 23 ns). The τ_d values, on the other hand, for **PPOCzPN**, **PPSCzPN** and **DiPPOCzPN** in 10 wt% mCP thin films were found to be 210 μs, 206 μs, and 54 μs, respectively, which are significantly shorter than those in PMMA and are also shorter than that of **2CzPN** (τ_d = 277 μs). An average τ_d of 273 μs has been reported previously for 6 wt% **2CzPN** in mCP thin film.[59] The excited state lifetime of the emitters doped in PMMA and mCP films are summarized in Table 3. Altogether, in contrast to **2CzPN**, the present data for **PPOCzPN**, **PPSCzPN** and **DiPPOCzPN** emitters clearly demonstrate the high sensitivity of the emitter decay dynamics and emission energy towards the nature of the host medium.

Temperature-dependent time-resolved emission decay measurements in 10 wt% doped mCP thin films are shown in Fig. S39 (ESI‡). There is a clear thermal activation of the delayed fluorescence that is consistent with compounds emitting *via* a TADF mechanism, despite the different trends in comparison to the PMMA matrix.

The singlet–triplet energy gaps (ΔE_{ST}) were determined from the difference in energy of the onset of the prompt fluorescence and phosphorescence spectra in 10 wt% doped mCP films measured at 77 K (Fig. 5). The ΔE_{ST} values for **PPOCzPN**, **PPSCzPN**, **DiPPOCzPN** and **2CzPN** were found to be 0.19 eV, 0.24 eV, 0.15 eV and 0.23 eV, respectively. The experimentally determined ΔE_{ST} value for **2CzPN** in 10 wt% doped mCP film is in good agreement with the reported value of 0.21 eV in a 6 wt% doped mCP thin film.[59,86] The smallest ΔE_{ST} value (0.15 eV for **DiPPOCzPN**) is consistent with the observed τ_d, value of 54 μs, which is the shortest among these emitters. It is noteworthy that the TD-DFT calculated ΔE_{ST} values in the gas phase are consistent with those experimentally determined in the apolar matrix, *vide infra*, Table 4. The ΔE_{ST} values determined for these chalcogenide-substituted **2CzPN** derivatives are of similar magnitude to literature **2CzPN** derivatives such as **α-2CbPN** (ΔE_{ST} = 0.28 eV) and **δ-2CbPN** (ΔE_{ST} = 0.13 eV) in 20 wt% mCP thin film, where α/δ-carboline was used as carbazole replacement to blue-shift the emission.[60]

3.3 Theoretical modelling

To better understand the differences between the PL behaviors observed in the polar DCM solvent or PMMA matrix *versus* the apolar toluene solvent or mCP matrix, our study has been complemented by quantum-chemical calculations. In line with our previous theoretical studies on TADF emitters,[86,90] we have first optimized the ground-state geometry of the **2CzPN** and its three derivatives in the gas phase at the Density Functional Theory (DFT) level using the PBE0 functional[91] and a 6-31G(d,p) basis set.[92] In a second step, we have analyzed the nature of the frontier electronic levels of the compounds. Finally, we have described the lowest singlet and triplet excited states of the emitters by performing TD-DFT calculations within the Tamm–Dancoff approximation,[93] employing the same functional and basis set.

In the case of the isolated **PPOCzPN** and **PPSCzPN** compounds, we have obtained two different low-energy conformers varying by the amplitude of the torsion angles ϕ between the carbazole and phthalonitrile units (see Fig. S40, ESI‡). For **PPOCzPN**, rotamer 2 with ϕ_1 = 134.3° and ϕ_2 =-69.2° is more stable by 0.29 eV compared to the other rotamer with ϕ_1 = −64.8° and ϕ_2 = −65.9°; in the case of **PPSCzPN**, there is a much larger difference of 1.33 eV between the most stable rotamer (with ϕ_1 = 133.2° and ϕ_2 = −69.5°) compared to the second rotamer (with ϕ_1 = −65.8° and ϕ_2 = −64.6°). In view of the large energy difference between the two rotamers (compared to the thermal energy, kT), their co-existence in solution most probably arises from their synthesis, rather than from thermal conversion following synthesis. We will discuss hereafter the properties of the most stable rotamer; for sake of completeness, the very similar properties computed for the second rotamer in the gas phase are collected in the ESI‡ (Fig. S40, S41 and Tables S2, S4). In contrast, we only found a single stable conformer for **2CzPN** and **DiPPOCzPN** with the

Table 3 Excited state lifetimes of the emitters doped in PMMA and mCP films

Emitter	10 wt% doped in PMMA films τ_p (%)/ns; τ_d (%)/μs	10 wt% doped in mCP films τ_p (%)/ns; τ_d (%)/μs	S_1/eV	T_1/eV
PPOCzPN	6.1 (43), 20.0 (57); 9 (3), 146 (22), 1024 (75)	10.0 (12), 37.2 (88); 20 (4), 90 (18), 522 (78)	2.96	2.77
PPSCzPN	5.8 (44), 13.6 (56); 5 (0.5), 174 (10), 1361 (90)	8.6, (44), 31.6 (56); 23 (4), 175 (33), 422 (62)	2.97	2.73
DiPPOCzPN	6.7 (40), 14.1 (60); 5 (2), 69 (6), 1176 (92)	8.1 (58), 26.4 (42); 0.5 (76), 28 (18), 136 (6)	2.96	2.81
2CzPN	8.3 (15), 21.1 (85); 6 (4), 124 (22), 680 (72)	9.9 (29), 23.2 (71); 7 (3), 134 (23), 690 (73)	2.90	2.67

S_1 = singlet state energy obtained from the onset of prompt fluorescence spectra measured at 77 K (λ_{exc} = 360 nm, delay time: 1 ns, time window: 1–100 ns). T_1 = triplet state energy obtained from the onset of the phosphorescence spectra measured at 77 K (λ_{exc} = 360 nm, delay time: 1 ms, time window: 1–10 ms).

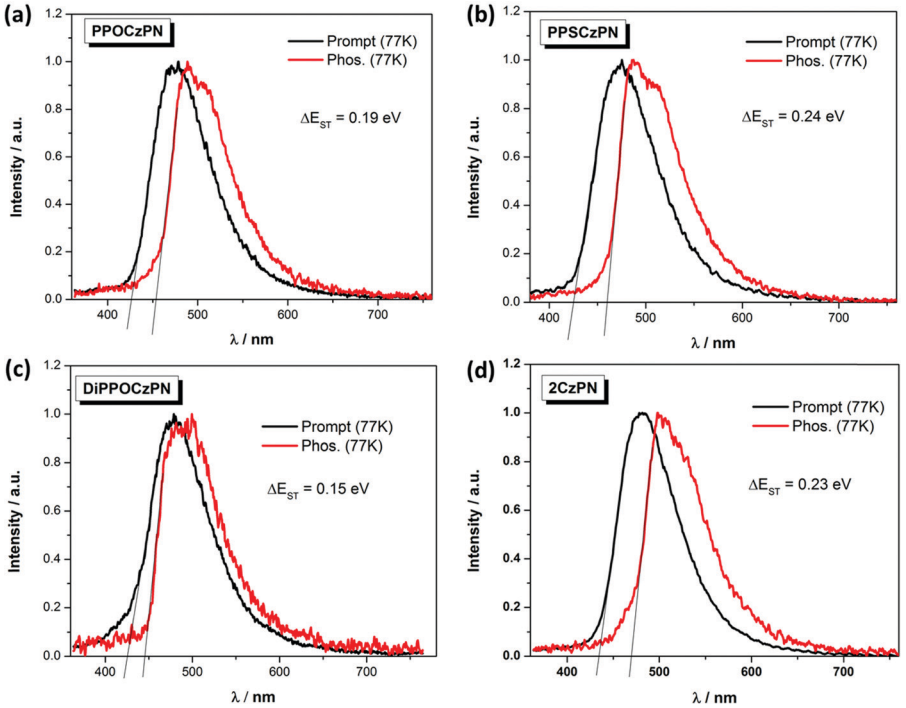

Fig. 5 Prompt fluorescence (at 77 K) and phosphorescence spectra (at 77 K) of (a) **PPOCzPN**, (b) **PPSCzPN**, (c) **DiPPOCzPN**, and (d) **2CzPN**, in 10 wt% doped mCP thin films (λ_{exc} = 360 nm).

same torsion angles for both carbazole substituents ($\phi_1 = \phi_2 = 58.9^\circ$ for **2CzPN** and $\phi_1 = \phi_2 = 65.7^\circ$ for **DiPPOCzPN**).

Table 4 collects the HOMO and LUMO energies of the four emitters calculated in the gas phase as well as in acetonitrile by modelling the solvent as a dielectric continuum using the Polarizable Continuum Model (PCM),[94] as implemented in Gaussian 16-A03;[95] in the latter case, the geometry is fully reoptimized within the PCM model, although this hardly changes the gas phase geometry. In acetonitrile, the HOMO is progressively stabilized going from **2CzPN** to **PPOCzPN** to **PPSCzPN** and **DiPPOCzPN**, which is generally consistent with the trends observed in the experimental electrochemistry data in DCM (Table 1) and acetonitrile (Fig. S36, ESI‡). On the other hand, the calculated LUMO energies vary to a lesser extent both according to the calculations and electrochemical measurements, as expected by the fact that the LUMO is localized on the phthalonitrile acceptor while the varying substituents are added on the donor fragment. Strikingly, the trends appear to be quite different when computing the frontier orbital energies in the gas phase, which is expected to reflect the properties in a non-polar medium such as toluene or the mCP matrix. The major difference is that the HOMO is not stabilized but in fact slightly destabilized when going from **2CzPN** to **PPOCzPN** or **PPSCzPN**, although it is stabilized going from **2CzPN** to **DiPPOCzPN**.

Table 4 Calculated HOMO and LUMO energies of **PPOCzPN**, **PPSCzPN**, **DiPPOCzPN** and **2CzPN** in gas phase *versus* MeCN

	In gas phase			In MeCN		
	HOMO/eV	LUMO/eV	ΔE/eV	HOMO/eV	LUMO/eV	ΔE/eV
PPOCzPN	−6.05	−2.52	3.53	−6.06	−2.48	3.58
PPSCzPN	−5.98	−2.58	3.40	−6.13	−2.50	3.63
DiPPOCzPN	−6.42	−2.73	3.69	−6.37	−2.57	3.80
2CzPN	−6.11	−2.41	3.70	−6.04	−2.39	3.65

The shape and energies of the orbitals in acetonitrile are displayed in Fig. 6 (and Fig. S41, ESI,‡ for the less stable rotamers of **PPOCzPN** and **PPSCzPN**). As expected, the HOMOs are mainly localized on the carbazole moieties, and the LUMOs are strongly localized on the phthalonitrile. In the mono-substituted compounds, the HOMO displays a small amount of electron density on the phosphine chalcogenide units, thus limiting the role played by mesomeric effects in defining the actual HOMO energies. The HOMO level is both the most delocalized in **DiPPOCzPN** and the most stabilized, which is also evidenced by its electrochemistry (Fig. 3 and Fig. S36, ESI‡). The shift of the HOMO among the compounds is a subtle interplay mostly between the inductively electron-withdrawing effects associated with the phosphine chalcogenide groups and electrostatic interactions between the polar phosphine chalcogenide and cyano moieties, which are expected to be further tuned by changes in the medium polarity. Altogether, the HOMO–LUMO gap in the gas phase is red shifted by 0.2–0.3 eV going from **2CzPN** to **PPOCzPN** and **PPSCzPN** while it remains unchanged for **DiPPOCzPN**. In contrast, the electronic bandgaps of **2CzPN**, **PPOCzPN**, **PPSCzPN** are quite similar in MeCN and larger by ∼0.2 eV for **DiPPOCzPN**, thus demonstrating the strong impact of the medium polarity on the electronic

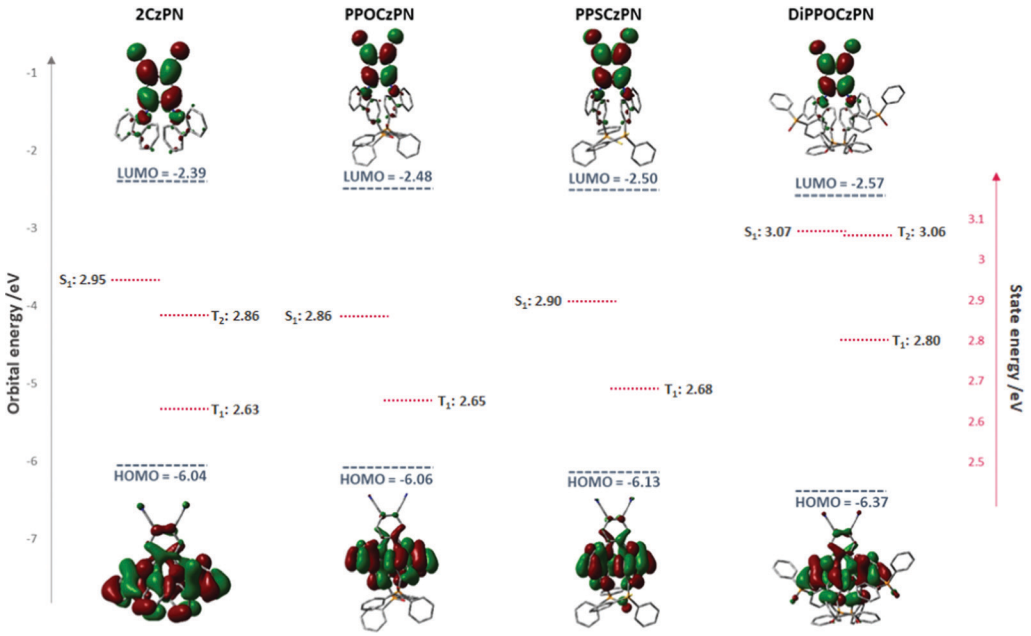

Fig. 6 HOMO and LUMO energies of the four compounds in their most stable geometries together with the energy of the lowest singlet and triplet excited states, as calculated in acetonitrile.

structure of the compounds and by extension on the charge-transfer state energies, as evidenced at the experimental level.

When coupled to a time-dependent (TD) formalism, DFT calculations can also give access to the excited-state photophysical properties of the emitters. We will describe below the excited state energies and associated oscillator strength (*f*) calculated in acetonitrile as well as the energy difference between T_1 and S_1 (Table 5) for vertical excitation processes (*i.e.* in the ground-state geometry). We will not address here at the theoretical level the changes in the emission properties as a function of the medium polarity evidenced experimentally, since a proper analysis would require a time-consuming optimization of the S_1 state (both in gas phase and in a polar medium described with PCM) which is often impeded by convergence problems and might require the use of another functional.[91] **PPOCzPN** and **PPSCzPN** exhibit a slightly red-shifted S_1 state compared to **2CzPN** (blue-shifted in the case of **DiPPOCzPN**), accompanied by a reduction in the oscillator strength, as well as slightly smaller ΔE_{ST} values. The calculated ΔE_{ST} values of the emitters in the toluene are all around or above 0.2 eV, in good consistency with those experimentally obtained in toluene (Table 2); there is a very good quantitative agreement for **2CzPN** (0.31 eV in theory *versus* 0.36 eV in toluene). These energies are marginally affected when performing the calculations in toluene or in acetonitrile (Table S4, ESI‡). Strikingly, the experimental ΔE_{ST} values are systematically reduced in the mCP matrix, most likely due in part to changes in the conformations of the emitters in these thin films. Both **2CzPN** and **DiPPOCzPN** have a second triplet excited state T_2 that lies below S_1, thus providing a conduit to facilitate reverse intersystem crossing process.[77,96] The T_1 and S_1 excited states are predominantly characterized by a HOMO–LUMO transition and hence both display a significant ICT character.

The absorption spectra simulated in the gas phase (Fig. S43, ESI‡) predict similar energy for the lowest absorption peaks (around 350 nm and 400 nm) for the four compounds; the same trends are also observed for the experimental spectra recorded both in MeCN and toluene (Fig. 4a and d). Note that the lowest absorption peak around 400 nm is systematically associated with higher-lying excited states while the lowest excited state S_1 gives rise to the shoulder on the low energy side. This state is mostly described by a HOMO to LUMO excitation. Analysis of the hole and electron densities (see typical plots for the gas phase in

Table 5 Excitation energies, ΔE_{ST}, oscillator strengths, and main component of the excitations in terms of one-electron transitions, as calculated in acetonitrile

Compound	States	Energy/eV	*f*	Main component of the excitation	Φ_s
PPOCzPN	T_1	2.65		HOMO → LUMO (76.5%)	0.60
	S_1	2.86	0.028	HOMO → LUMO (97.7%)	0.35
	ΔE_{ST}	0.21			
PPSCzPN	T_1	2.68		HOMO → LUMO (80.5%)	0.61
	S_1	2.90	0.032	HOMO → LUMO (97.9%)	0.37
	ΔE_{ST}	0.22			
DiPPOCzPN	T_1	2.80		HOMO → LUMO (82.1%)	0.66
	T_2	3.06			0.50
	S_1	3.07	0.045	HOMO → LUMO (98.3%)	0.39
	ΔE_{ST}	0.27			
2CzPN	T_1	2.63		HOMO → LUMO (87.8%)	0.66
	T_2	2.86			0.53
	S_1	2.95	0.100	HOMO → LUMO (98.4%)	0.43
	ΔE_{ST}	0.32			

Fig. S42, ESI‡) obtained within the attachment/detachment formalism points to a similar charge transfer character in the S_1 state of the four compounds in acetonitrile or in gas phase (Table 5); the overlap index ϕ_S, ranging from 1 for a pure locally excited state (LE) to 0 for a pure charge-transfer (CT) state, is around 0.4 in all cases, *i.e.*, an indication of a hybrid state with significant LE and CT character. The T_1 state exhibits systematically a higher ϕ_S index pointing to a more local excited state. This change in character between the S_1 and T_1 (T_2) states ensures non-vanishing spin–orbit coupling based on El Sayed's rules and opens up the RISC channel.

3.4 Electrochemiluminescence *via* the Annihilation pathway

ECL is luminescence generated when electrochemically-generated radical cations (hole) and radical anions (electron) undergo an electron transfer to create an excited state (exciton), which can release its energy as light (Fig. 7a). The behavior of this luminescence can describe radical stability, reactivity and general emission mechanisms of luminophores at concentrations that are typically greater than that in solutions used in photoluminescence studies. Radical cations and anions are produced in solution when the species are oxidized and reduced, respectively in the vicinity of the same working electrode. If these two species collide, an electron transfer can happen from the HOMO (or LUMO) of a radical anion to the HOMO (or LUMO) of a radical cation, potentially creating an exciton that can subsequently emit light in the form of ECL. This mechanism is not limited to the generation of triplets as illustrated in Fig. 7a, but also can form systematically singlets in the case of an annihilation mechanism, in an analogous manner to exciton generation in an organic light-emitting diode. We note that it is unlikely for radicals to undergo further redox reactions at an electrode surface to create excited state species as described in the literature.[97] In fact, the electrode surface might quench the radical or excited species.

To electrogenerate an excited state, the electronic gap of the redox reactions (EE_g) must be greater than the photoluminescence emission peak energy (E_g) as defined by eqn (2). For an ECL annihilation system, R' and R are the same species. However, R' can become a radical while R remains the luminophore in an oxidative-reduction ECL co-reactant system or R can become an oxidant while R' remains a luminophore in a reductive-oxidation ECL co-reactant system. Using eqn (2), the electronic gap for **PPOCzPN**, **PPSCzPN** and **DiPPOCzPN** in DCM are measured to be 2.73, 2.98 and 3.19 eV, respectively, from the redox potentials in differential pulse voltammograms (Fig. S35, ESI‡). From the prompt fluorescence spectra in DCM in Fig. 5, the optical gap for **PPOCzPN**, **PPSCzPN** and **DiPPOCzPN** are 2.49, 2.47 and 2.66 eV, respectively. As expected, the energy provided by the redox reactions for all compounds is sufficient to generate both singlet and triplet excited states. The blue curves in Fig. 3a–c demonstrate ECL generated during scan cycles between redox reaction potentials for **PPOCzPN**, **PPSCzPN** and **DiPPOCzPN**. **DiPPOCzPN** shows a maximum ECL intensity of 60 nA, while **PPOCzPN** and **PPSCzPN** display weak emissions up to 1 nA. This indicates that the radical cation is sufficiently stable to survive in solution until the radical anion is created, and the two species collide. **DiPPOCzPN**$^{\bullet+}$ is the most stable radical ion because it produced the highest ECL emission in the annihilation pathway. It also appears that the radical anion is not as stable as the radical cation for all species, because no ECL is seen upon first reduction of the species followed by compound oxidation, even after multiple cycles. The irreversibility of the oxidation reaction shown in CVs might be caused by the potential window limit of the DCM electrolyte solution as can be seen from the CVs in MeCN, Fig. S37 (ESI‡).

Fig. 3d–f shows ECL-time curves during pulsing between 0.1 V more anodic than the oxidation and 0.1 V more cathodic than reduction peak potentials, respectively. **PPOCzPN**, **PPSCzPN** and **DiPPOCzPN** yielded annihilation ECL maxima at 700, 1100 and 17 500 nA, respectively. In pulsing experiments, the time between the generation of both radical species in solution is shorter than that in potential cycling, allowing the lifetime of the radical not to be a significant issue and the annihilation ECL to be enhanced. The pulsing annihilation efficiency was determined by eqn (1) where *x* and *st* stand for

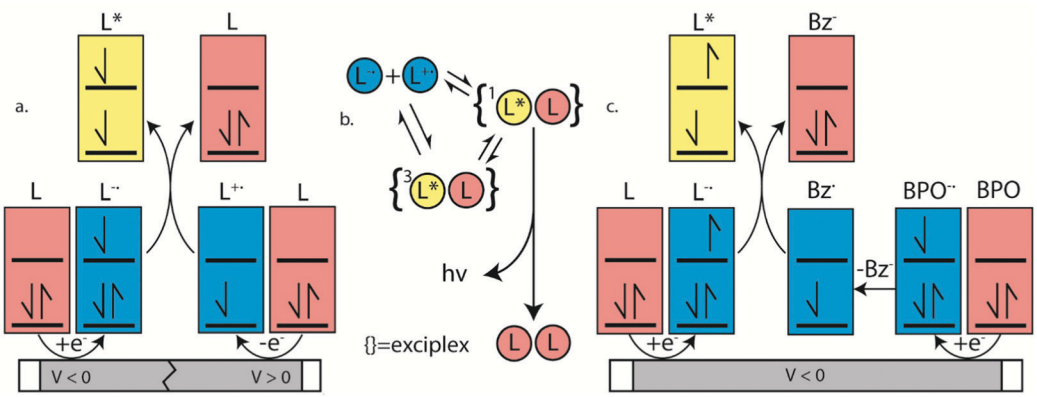

Fig. 7 (a) Annihilation and (c) benzoyl peroxide (BPO) co-reactant mechanisms for ECL emission. L, benzoic acid (Bz) and BPO stand for luminophore, benzoate and benzoyl peroxide, respectively. This scheme is illustrative and not energy accurate. Both triplet and singlet energy states can be accessed from either co-reactant or annihilation mechanisms. (b) Diagram illustrating excimer formation and the equilibrium established between anionic and cationic radicals.

Table 6 Summary of ECL data

	PPOCzPN	PPSCzPN	DiPPOCzPN	$[Ru(bpy)_3]^{2+}$
EE_g (eV)[a]	2.73	2.98	3.19	2.55
Pulsing ECL_{onset} delay (ms)[b]	7	14	11	0
Pulsing ECL_{max} delay (ms)[b]	11	19	24	4
Pulsing ECL efficiency (%)[c]	1	1	10	100
Max pulsing ECL (nA)	700	1150	17 500	70 000
Annihilation ECL λ_{max} (nm)	520	500	475	620
EE_g BPO (eV)[d]	3.01	3.48	3.39	3.04
BPO ECL efficiency (%)[c]	17	6	1	100
Max BPO ECL (nA)	3200	1280	80	26 500
BPO ECL λ_{max} (nm)	520	500	545	620

[a] Electronic gaps (EE_g) were obtained using eqn (2) and the differential pulse voltammograms of the compounds in Fig. S36. [b] These values are averages from at least 40 pulses with individual conditions described in Fig. 3. [c] Obtained from eqn (1) relative to $[Ru(bpy)_3]^{2+}$ at the same concentration, electrolyte and concentration of co-reactant if applicable. [d] Obtained from eqn (2) but with substituting $E^{\circ}(R^{\bullet+}/R')$ with the oxidative power of BPO from ref. 98.

the luminophore and $[Ru(bpy)_3]^{2+}$ under the same conditions, respectively. These ECL efficiencies were determined to be 1, 1 and 10% relative to $[Ru(bpy)_3]^{2+}$, for **PPOCzPN**, **PPSCzPN** and **DiPPOCzPN**, respectively (Table 6). Interestingly, **2CzPN** showed no emissions in the annihilation pathway as seen in Fig. S38a and b (ESI‡). **DiPPOCzPN** continued to have the highest ECL maxima and also had the most efficient emission; interestingly, the structurally similar **PPOCzPN** had the lowest efficiency. Most emission was observed when a negative potential was applied, further providing evidence for the higher stability of the radical cation over the radical anion. In fact, **PPOCzPN** is the only species to display emission when a positive potential was applied or when radical cations were actively being produced in pulsing experiments (Fig. 3d–f), indicating a relatively high radical anion reactivity, or a relatively lower radical cation reactivity than the other compounds. For optoelectronic applications, ECL efficiency, ECL maxima, radical stability and radical reactivity are all important parameters to consider. Inequalities between radical cation and radical anion stabilities and reactivities can cause excess charge buildup in OLEDs, leading to fast device degradation. High ECL maxima and efficiencies indicate efficient charge transfers as well as limited non-radiative decay pathways. Therefore, **PPOCzPN** appears desirable for optoelectronic applications because of relatively more stable and reactive radical ion species, although it has low ECL maxima and efficiency.

After several pulses, the emission intensity of **DiPPOCzPN** decreases by over 75%, whereas **PPOCzPN** and **PPSCzPN** remain relatively stable over the same time (Fig. S45, ESI‡). It appears that **DiPPOCzPN** may form side products during the annihilation pulsed ECL experiment that influence the generation of excited species. This fast decay may also be caused by a charge imbalance where negatively or positively charged species that accumulate over time interfere with the exciton states, similar to exciton–polaron quenching of excited states.[99]

Average ECL onset times. These experiments reveal for the first time (Fig. 3d–f) that there is a delay in the ECL onset times (ECL_{onset}) from donor–acceptor TADF compounds; **PPOCzPN**, **PPSCzPN** and **DiPPOCzPN** had 7 (26 pulses measured), 14 (36 pulses measured) and 11 ms (37 pulses measured) initial ECL delays, respectively. The data are summarized in Table 6 and zoom-in ECL-time curves of a single pulse of each compound are shown in Fig. S46 (ESI‡). The slow kinetics of the formation of an excimer between the radical cation and radical anion of these compounds may cause this delay as illustrated in Fig. 6.

We first considered phosphorescence as the origin of these long ECL onset times. For time comparisons of diffusion properties and emissions, the well-studied commercial phosphorescent ECL emitter $[Ru(bpy)_3]^{2+}$,[100–103] was tested under the same conditions (Fig. S47, ESI‡) and showed no observed delay (47 pulses measured). A well-studied organic compound with a known diffusion coefficient is diphenylanthracene (DPA) ($D_{ACN} = 0.20 \times 10^{-6}$ cm^2 s^{-1}),[104] which shows an order of magnitude difference between its diffusion coefficient and that of $[Ru(bpy)_3]^{2+}$ ($D_{ACN} = 5.8 \times 10^{-6}$ cm^2 s^{-1}).[105] If we assume that DPA and these **2CzPN** derivatives have similar magnitudes of diffusion coefficient in DCM, from a comparison of their initial emission delays (7 and 0 ms for **PPOCzPN** and $[Ru(bpy)_3]^{2+}$, respectively), differences in diffusion rates can be ruled out as a cause of emission delays in the **2CzPN** derivatives. We believe diffusion delays are on the time scale of microseconds and cannot explain the observed time delay shown in Fig. 3d–f.

We next considered triplet–triplet annihilation as the origin for the long ECL onset times. A TTA mechanism has been used to explain millisecond photoluminescence lifetimes for phenanthrene and may explain the delay of the onset of the ECL seen here.[106] Also, the competition for triplet exciton depopulation by TTA, RISC and non-radiative pathways has been studied by Grüne *et al.* in a m-MTDATA:3TPYMB exciplex TADF OLED to estimate that TTA was responsible for 50% of triplet depopulation, which effectively extended the emission decay time.[107] However, Grüne *et al.* excited their sample for 4 ms at a specific current density and did not see any delay in the onset of emission. TTA has been observed in carbazolyl phthalonitrile derivatives where there is an observed blue-shifting in the solid-state PL as well as serious efficiency roll-off in the OLEDs,[108,109] but to the best of our knowledge it has not been demonstrated before by ECL in **2CzPN** derivatives. Mechanistically, TTA can be simplified to two triplet excitons (T_1) combining to form a singlet exciton (S_n) seen in Fig. 7b. The system in the S_n state then relaxes to the S_1 state by internal conversion according to Kasha's law, which can then emit light. TTA is also a common tetramolecular process in ECL where the radical cation of *N*,*N*,*N*′,*N*′-tetramethyl-*p*-phenylenediamine ($TMPD^{\bullet+}$) and the radical anion of DPA ($DPA^{\bullet-}$) reside as a well-studied purely TTA-emitting ECL system.[68,98,110,111] This $TMPD^{\bullet+}/DPA^{\bullet-}$ system can only generate T_1 from charge transfer reactions and not S_1 as dictated by eqn (2). However, this TTA mechanism has

never been accompanied by an observed induction time either in ECL or OLED prior to observed emission.

To the best of our knowledge, there has only been one study of emission delay after excitation in an ECL system, where the ECL of DPA was found to have a delay on the order of 100 μs.[112] This delay was attributed to uncompensated solution resistance. In comparison, our experiment also has a platinum working electrode with the same electrolyte (TBAP) at a similar concentration, but the delay we determined is a few orders of magnitude larger than what Rosenmund *et al.* observed. Thus, neither uncompensated solution resistance, nor triplet–triplet annihilation (TTA), nor phosphorescence is responsible and that this ECL emission delay is currently unexplained in the literature.

Interestingly, an organic long-persistent photoluminescence (OLPL) phenomenon was recently discovered by Kabe *et al.* in a system comprising a phosphine oxide-containing TADF acceptor (2,8-bis(diphenylphosphoryl)dibenzo-[*b*,*d*]thiophene) (PPT)) and *N*,*N*,*N*′,*N*′-tettramethylbenzidine (TMB) as a donor molecule.[113] More recently, this OLPL system has been used in an OLED to achieve organic long-persistent electroluminescence (OLEL).[114,115] Unfortunately, solution and solid state emission delays of the system were not investigated on time scales smaller than 1 s, thereby limiting comparisons with the **2CzPN** derivatives. However, OLPL and OLEL are both emitted from an exciplex state and therefore the emission was found to be both concentration dependent and layer-thickness dependent. This exciplex emission was also found to have thermal activation processes and thermoluminescence in films.[115] Li *et al.* reported that the TADF emitter, **CzPhAP**, did not show any delay in the onset of emission but did show 900 s of persistent emission after 60 s of laser excitation, when cast in a PMMA film.[116] These unusually long emission times were ascribed to slow charge recombination rates of the luminophore in the thick film, leading to organic long-persistent photoluminescence (OLPL) because of an established equilibrium between exciplex formation with radicals and the subsequent radical disassociation. We thus contend that the delay in the onset of the ECL emission seen in Fig. 3d–f may be best explained by a heretofore previously unreported organic long-persistent electrochemiluminescence (OLECL), analogous to the works of Kabe *et al.* We hypothesize that an equilibrium exists between the emissive excimer and the dissociated constituents and that the slow association kinetics could cause this delay as illustrated in Fig. 7b.

Average ECL rising times to maximum. The average times from the onset of ECL to the ECL emission maximum after a pulse for **PPOCzPN**, **PPSCzPN** and **DiPPOCzPN** were found to be 11 (78 pulses measured), 19 (37 pulses measured) and 24 ms (77 pulses measured), respectively (Fig. 3d–f and Table 6). Again, for comparison, $[Ru(bpy)_3]^{2+}$ was analyzed using the same ECL pulsing method and this compound shows a rise time of 4 ms (158 pulses measured, Fig. S47, ESI‡). Notably, the magnitude of the delay in reaching the maximum ECL emission intensity (Table 6) correlates with the trends in ΔE_{ST} values in toluene (Table 2), where **PPOCzPN** has the smallest ΔE_{ST} at 0.20 eV, and **PPSCzPN** and **DiPPOCzPN** have the largest ΔE_{ST} at 0.42 and 0.43 eV, respectively (Fig. 8). Based on this relationship, we can confidently rule out TTA as a dominant emission mechanism. Interestingly, the OLPL TADF emitter **CzPhAP** mentioned earlier had a similarly large ΔE_{ST} of 0.18 eV compared with **PPOCzPN** (Table 2).

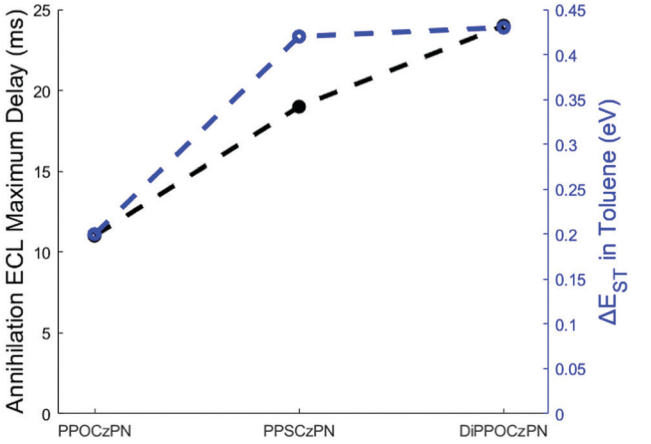

Fig. 8 A relationship between the ΔE_{ST} in toluene and the annihilation ECL maximum delay of the **2CzPN** derivatives in this study.

Average long emission decay time. The average long emission decay time after switching off pulses was measured to find how long it took ECL emission to return to 0 nA after the potential is switched off (Fig. 3d–f and Fig. S47, ESI‡). These long emission decay times were found to be 0, 6, and 6 ms for **PPOCzPN**, **PPSCzPN** and **DiPPOCzPN**, respectively. Expectedly, the same trends for the delay to the onset of ECL and the time required from the ECL onset to reach a maximum ECL intensity were observed. However, the ECL decay times were roughly half the magnitude of the ECL onset times. By contrast, $[Ru(bpy)_3]^{2+}$ shows instantaneous ECL emission during both cathodic and anodic pulses (Fig. S47, ESI‡), and rapid decay of the ECL emission, which could not be quantified.

3.5 ECL of BPO Co-reactant systems

Benzoyl peroxide (BPO) was added as a co-reactant to the electrochemical systems described in Fig. 3 and the potential was scanned in the cathodic direction. This co-reactant pathway is described in Fig. 7c. Around −0.45 V *vs.* SCE, BPO is reduced and ultimately decomposes into a benzoate radical (Fig. 7c). When **PPOCzPN**, **PPSCzPN** and **DiPPOCzPN** are subsequently reduced to form **PPOCzPN**$^{\bullet-}$, **PPSCzPN**$^{\bullet-}$ and **DiPPOCzPN**$^{\bullet-}$, the benzoate radical produced earlier can abstract an electron from the HOMOs of the reduced TADF compounds to produce excited states **PPOCzPN***, **PPSCzPN*** and **DiPPOCzPN***, respectively. These excited-state compounds then emit ECL through the so-called co-reactant pathway. Fig. 9a–c show the reduction waves corresponding to the reduction of BPO (red traces) and the corresponding photocurrent generated (blue traces). ECL intensity maxima of 3000, 1280 and 80 nA were measured for **PPOCzPN**, **PPSCzPN** and **DiPPOCzPN**, respectively. **PPOCzPN** showed the strongest ECL

response, which was almost three-fold stronger than that of **PPSCzPN** and 38 times that of **DiPPOCzPN**. From previous theoretical and experimental studies,[98] benzoate radicals have a redox potential of 1.5 V, which is sufficient to oxidize the three TADF compounds in this study, and for this co-reactant ECL pathway to provide more energy than the annihilation ECL pathway. The difference in emission intensities compared to the annihilation pathway is likely due to this available energy increase.

The BPO co-reactant ECL efficiencies for **PPOCzPN**, **PPSCzPN** and **DiPPOCzPN** were determined to be 17, 6 and 1%, respectively, using eqn (1) (Table 6). Interestingly, this ECL efficiency difference between **PPOCzPN** and **DiPPOCzPN** resembles the difference in Φ_{PL} for the emitters in a PMMA film (56 to 28%) more than it does the Φ_{PL} difference in DCM (51 to 61%). This indicates that the ECL co-reactant pathway for **DiPPOCzPN** has an additional non-radiative decay pathway. In ECL co-reactant systems, the lifetime of the radical poses less of an issue than in annihilation experiments, since radical reactants are generated almost simultaneously, typically allowing ECL enhancement in solution. Now that radical stability is less of a factor, **PPOCzPN**$^{\bullet-}$ appears to have a higher reactivity than **DiPPOCzPN**$^{\bullet-}$ and **PPSCzPN**$^{\bullet-}$ towards BPO. A higher anion reactivity for **PPOCzPN** was noted during pulsing experiments (Fig. 3d–f) and appears to have been observed again in the BPO experiments. With increased available energy, it appears that **PPOCzPN** is the strongest emitter and maintains its position as the best candidate for optoelectronics.

3.6 ECL spectroscopy

Fig. 9d–f show spooling ECL spectroscopy performed on all co-reactant systems described herein. The ECL spooling spectra add a new data dimension of wavelength to the same spectra seen in Fig. 9a–c. The BPO co-reactant systems show a light green emission for all species with maximum emission CIE coordinates of (0.29,0.40), (0.31,0.42) and (0.33,0.38) for **PPOCzPN**, **PPSCzPN** and **DiPPOCzPN**, respectively. In contrast to the annihilation pathway and also observed in the PL study, the **DiPPOCzPN**/BPO co-reactant system has the most red-shifted emission spectrum (Table 4 and Fig. 9f), rather than the most blue-shifted. This large red-shift and relative drop in efficiency indicate that **DiPPOCzPN** may suffer from exciplex formation under these conditions. Exciplexes are heterodimeric species created by intermolecular interactions between a hole on the donor moiety of one molecule and the electron on the acceptor moiety of a second molecule.[117] Exciplexes typically have smaller HOMO–LUMO gaps than either of the constituent components, thereby resulting in an observed red-shifted

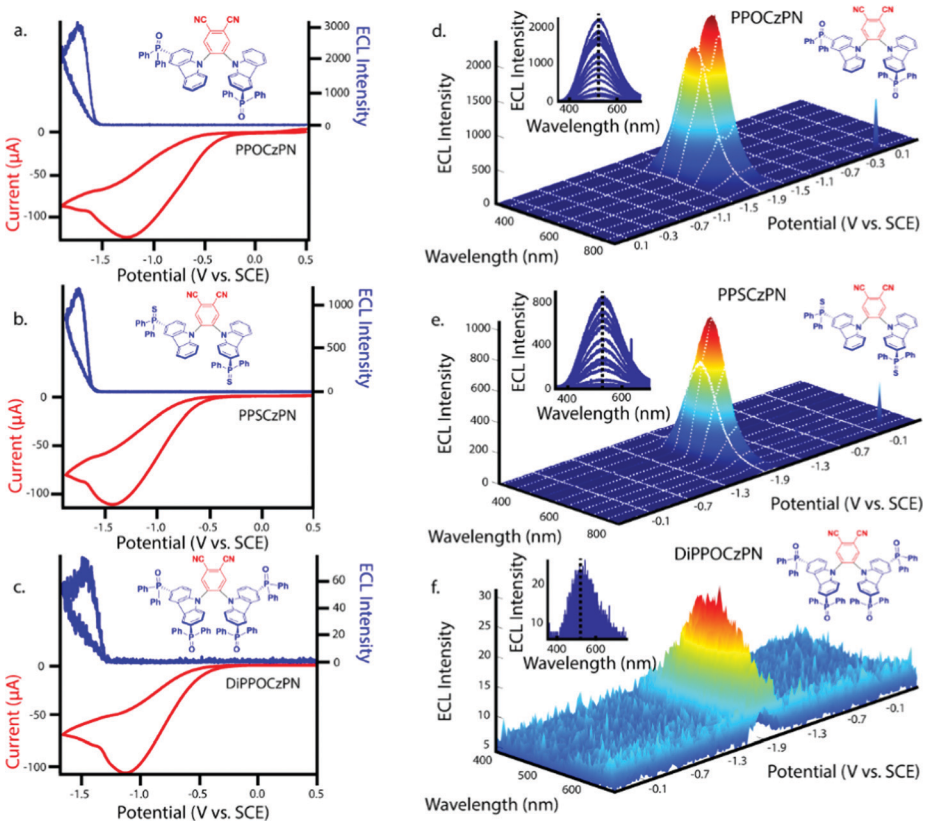

Fig. 9 (a–c) CVs (red) along with ECL–voltage curves (blue) during potential pulsing at a pulsing frequency of 10 Hz for **PPOCzPN**, **PPSCzPN** and **DiPPOCzPN**, respectively, all with 10 mM BPO was added as a co-reactant. (d–f) Spooling ECL spectroscopy of the corresponding systems described in Figures a–c. Insets of Figures d–f represent respective stacked spooling ECL spectra. The purple color of these insets was arbitrarily chosen but Fig. S48 (ESI‡) displays the observable color of each recorded spectrum.

emission. Exciplex formation in OLEDs with luminophores substituted by diphenyl phosphine oxide substituents have been reported by Tourneur *et al.*, who harnessed this exciplex formation to produce emissions from both intramolecular and intermolecular charge-transfer states yielding white light OLEDs.[118] The exciplex identified during **DiPPOCzPN**/BPO co-reactant analysis appears not to be affected by an increasing concentration of reduced species in the vicinity of the electrode, since as the cyclic voltammogram progresses, no shift in emission maxima is seen (insets of Fig. 9d–f with expansions of the insets in Fig. S48, ESI‡). Additionally, there was no identified exciplex formation during the annihilation studies with **DiPPOCzPN**. The most probable explanation for the observed red-shifted emission is due to the exciplex between **DiPPOCzPN**$^{\bullet-}$ and Bz$^{\bullet+}$. Newcomb *et al.* has identified the necessity to screen potential TADF OLED emitters for exciplex formation, as the presence of exciplexes was shown to lower device lifetime.[119] Masui *et al.* also identified large EQE roll-off in OLEDs caused by charge imbalance in the emissive layer that are exacerbated at higher current densities.[109,120] The exciplex formation in these compounds is characteristic of compounds that also exhibit OLPL, thereby supporting OLECL emission as the dominant mechanism. Interestingly, the longest pulsing ECL_{onset} delay belonged to **DiPPOCzPN**, which was the only compound to form a very evident exciplex during BPO co-reactant analysis. Interestingly, **2CzPN** showed emissions centered at 550 nm, resembling the emissions seen in the **DiPPOCzPN**/BPO coreactant studies in Fig. S38c and d (ESI‡). This center wavelength is also 50 nm red-shifted from the **2CzPN** PL studies likely due to a similar exciplex formation.

In a similar manner to the BPO co-reactant, 5 mM tripropylamine (TPrA) was added as an alternative co-reactant (Fig. S49 and S50, ESI‡). A thorough discussion of the TPrA co-reactant systems follows Fig. S49 (ESI‡) in the ESI.‡ Under these conditions, the **PPSCzPN**/TPrA system behaved in the exact same manner as the **DiPPOCzPN**/BPO system, likely indicating a similar exciplex formation. There were no excimers identified in the **PPSCzPN** annihilation mechanism, indicating that the interactions between **PPSCzPN**$^{\bullet+}$ and **NPr3**$^{\bullet}$ may be responsible for the exciplex formation. The **PPSCzPN**/TPrA system also seems to be concentration-dependent where an increasing overpotential that creates more **PPSCzPN**$^{\bullet+}$ in the vicinity of the electrode gradually causes a red-shift. The compounds with the longest onset to ECL emission, longest time to achieve a maximum ECL intensity, longest ECL decay time, largest ΔE_{ST} and weakest ECL efficiencies likely form exciplexes under co-reactant conditions. These correlations and relationships all support the putative OLECL emission mechanism.

In Fig. 10, the normalized accumulation spectra of all ECL processes discussed so far are overlapped, with ECL peak wavelengths summarized in Table 6. A slight red-shift is seen for all ECL emissions relative to the PL emissions, which is likely due to the more concentrated solutions used in the ECL measurements that result in increased self-absorption of the higher energy components of the emission spectra in the ECL studies. The PL and ECL spectra for **PPOCzPN** do not shift,

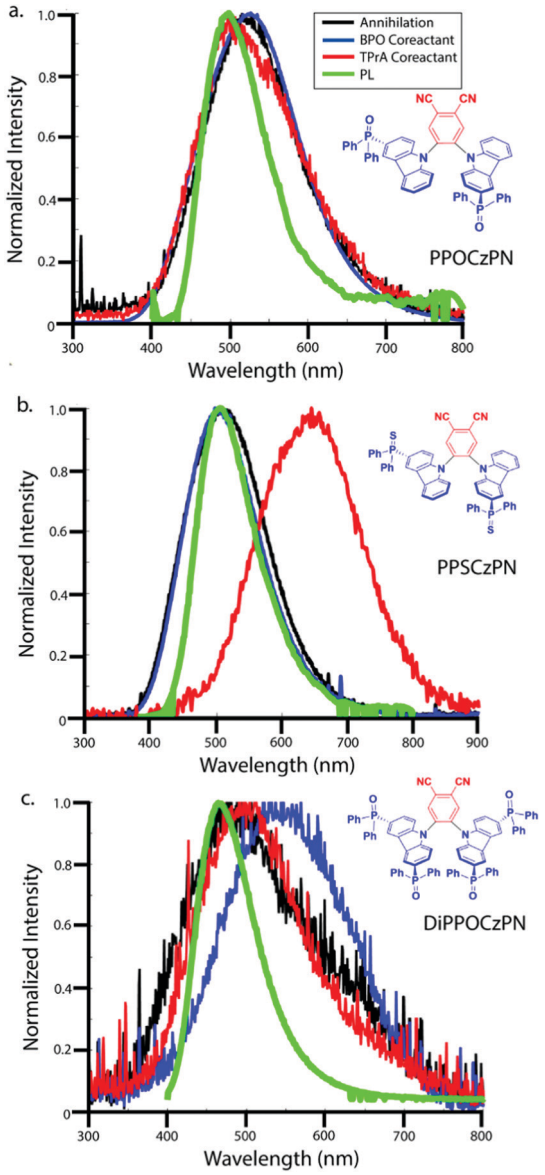

Fig. 10 Accumulated ECL spectra during different light generation methods. The annihilation ECL, BPO co-reactant ECL, TPrA co-reactant ECL and photoluminescence emissions are colored in black, blue, red and green traces for (a) **PPOCzPN**, (b) **PPSCzPN** and (c) **DiPPOCzPN**, respectively.

indicating a common excited state accessed in all processes. However, there is a large red-shift observed for both the **DiPPOCzPN**/BPO co-reactant pathway and for the **PPSCzPN**/TPrA co-reactant pathway. These red-shifts in the ECL spectra typically indicate exciplex formation.

4. Conclusions

Herein, we detailed the synthesis and characterization of three new **2CzPN** derivatives with phosphine chalcogenide oxide groups substituted on the donor moiety. This strategy successfully stabilized the HOMO level of the donor, confirmed by

cyclic voltammetry. By extension, the lowest-lying charge-transfer state was shifted to higher energy, thereby promoting a deeper blue emission, confirmed by photoluminescence studies. Surprisingly, the same trends are not recovered when measuring emissions in apolar media, thus highlighting solvatochromic effects on the TADF properties of the **2CzPN** derivatives. Quantum-chemical calculations support these solvatochromic observations. Electrochemiluminescence studies in the desirable polar medium revealed a heretofore undocumented emission mechanism under electrical excitation in solution. Delayed ECL onset times relative to common ECL emitters in annihilation pathway revealed that organic long-persistent emission was operational and that the delay in the onset times correlated with the ΔE_{ST} of the emitters. **PPOCzPN**, which has the smallest ΔE_{ST}, yielded the strongest, fastest, and most efficient ECL emissions when using BPO co-reactant. Thus, this compound should be the most suitable for optoelectronic applications after considering radical stability, emission stability, emission efficiency and emission intensity. Studies on ECL spooling spectroscopy and accumulated ECL spectroscopy identified that an exciplex of **DiPPOCzPN** forms while in the presence of radical anions. Analogous to the OLPL mechanism advanced by Kabe *et al.* the slow kinetics of exciplex formation and subsequent emission are likely responsible for the OLECL in this case. This work reveals a heretofore unknown ECL emission mechanism, OLECL, that manifests in both very long onset of ECL emission and long ECL lifetimes. Our study also provides significantly more detailed insight into the ECL of TADF compounds, which can be used to guide and screen TADF compound suitability for optoelectronic applications such as OLEDs.

Author contributions

S. K., M. Y. W., and E. Z.-C. designed and synthesized the materials. S. K., P. R. and P. T. carried out the photophysical study. J. R. A and Z. D. performed the electrochemical and ECL studies. D. B. C. and A. M. Z. S. solved the structure of the single crystals. P. T., Y. O., J. C., R. L., and P. V. carried out the theoretical modeling. S. K., E. Z.-C., J. R. A., Z. D., P. T., Y. O., J. C. wrote the manuscript. Y. O., J. C., Z. D. and E. Z.-C. supervised the project.

Abbreviations

TADF	Thermally activated delayed fluorescence;
ECL	Electrochemiluminescence
2CzPN	4,5-Dicarbazolylphthalonitrile
BPO	Benzoyl peroxide
TPrA	Tripropylamine
HOMO	Highest occupied molecular orbital
LUMO	Lowest unoccupied molecular orbital
OLPL	Organic long-persistent photoluminescence
OLECL	Organic long-persistent electrochemiluminescence
TTA	Triplet–triplet annihilation
RISC	Reverse intersystem crossing
LE	Locally excited
CT	Charge transfer
DFT	Density functional theory
CV	Cyclic voltammetry
DPV	Differential pulse voltammetry.

Conflicts of interest

There are no conflicts to declare.

Acknowledgements

The authors thank Dr Sai Kiran Rajendran for providing PL and TCSPC data of **2CzPN** in neat film. SK acknowledges the financial support from European Union's Horizon 2020 research and innovation programme under Marie Skłodowska Curie Individual Fellowship (MCIF; Agreement No. 748430-THF-OLED). P. R acknowledges support from a Marie Skłodowska-Curie Individual Fellowship (No. 749557). We thank the EPSRC UK National Mass Spectrometry Facility at Swansea University for analytical services. The work has been supported in Mons by European Union through the Interreg V initiative France-Wallonie-Vlaanderen project LUMINOPTEX and the Belgian National Fund for Scientific Research (FRS-FNRS). Computational resources were provided by the Consortium des Équipements de Calcul Intensif (CÉCI) funded by F. R. S.-FNRS under Grant 2.5020.11. J. C. is an FNRS research director. Y. O. acknowledges funding by the Fonds de la Recherche Scientifique-FNRS under Grant no F.4534.21 (MIS-IMAGINE). We acknowledge the research support from Natural Sciences and Engineering Research Council Canada (NSERC, DG RGPIN-2013-201697, DG RGPIN-2018-06556, and SPG STPGP-2016-493924), Canada Foundation of Innovation, Ontario Innovation Trust (CFI/OIT, 9040) and Western University. J. R. A. appreciates the Ontario graduate scholarships (2018–2022). EZ-C is a Royal Society Leverhulme Trust Senior Research fellow (SRF\R1\201089). For the purpose of open access, the authors have applied a Creative Commons Attribution (CC BY) license.

References

1 Y. Sun, N. C. Giebink, H. Kanno, B. Ma, M. E. Thompson and S. R. Forrest, Management of Singlet and Triplet Excitons for Efficient White Organic Light-Emitting Devices, *Nature*, 2006, **440**, 908–912.
2 C. Adachi, M. A. Baldo, M. E. Thompson and S. R. Forrest, Nearly 100% internal phosphorescence efficiency in an organic light-emitting device, *J. Appl. Phys.*, 2001, **90**, 5048–5051.
3 K. P. Klubek, C. W. Tang and L. J. Rothberg, Investigation of Blue Phosphorescent Organic Light-Emitting Diode Host and Dopant Stability, *Org. Electron.*, 2014, **15**, 1312–1316.

4 T. Huang, W. Jiang and L. Duan, Recent Progress in Solution Processable TADF Materials for Organic Light-Emitting Diodes, *J. Mater. Chem. C*, 2018, **6**, 5577–5596.
5 X.-K. Chen, D. Kim and J.-L. Brédas, Thermally Activated Delayed Fluorescence (TADF) Path Toward Efficient Electroluminescence in Purely Organic Materials: Molecular Level Insight, *Acc. Chem. Res.*, 2018, **51**, 2215–2224.
6 S. K. Jeon, H. L. Lee, K. S. Yook and J. Y. Lee, Recent Progress of the Lifetime of Organic Light-Emitting Diodes Based on Thermally Activated Delayed Fluorescent Material, *Adv. Mater.*, 2019, **31**, 1803524.
7 M. Godumala, S. Choi, M. J. Cho and D. H. Choi, Recent Breakthroughs in Thermally Activated Delayed Fluorescence Organic Light Emitting Diodes Containing Non-Doped Emitting Layers, *J. Mater. Chem. C*, 2019, **7**, 2172–2198.
8 P. Data and Y. Takeda, Recent Advancements in and the Future of Organic Emitters: TADF- and RTP-Active Multifunctional Organic Materials, *Chem. – Asian J.*, 2019, **14**, 1613–1636.
9 Y. Olivier, J. C. Sancho-Garcia, L. Muccioli, G. D'Avino and D. Beljonne, Computational Design of Thermally Activated Delayed Fluorescence Materials: The Challenges Ahead, *J. Phys. Chem. Lett.*, 2018, **9**, 6149–6163.
10 H. Uoyama, K. Goushi, K. Shizu, H. Nomura and C. Adachi, Highly Efficient Organic Light Emitting Diodes from Delayed Fluorescence, *Nature*, 2012, **492**, 234–238.
11 P. de Silva, C. A. Kim, T. Zhu and T. Van Voorhis, Extracting Design Principles for Efficient Thermally Activated Delayed Fluorescence (TADF) from a Simple Four-State Model, *Chem. Mater.*, 2019, **31**, 6995–7006.
12 R. S. Nobuyasu, Z. Ren, G. C. Griffiths, A. S. Batsanov, P. Data, S. Yan, A. P. Monkman, M. R. Bryce and F. B. Dias, Rational Design of TADF Polymers Using a Donor–Acceptor Monomer with Enhanced TADF Efficiency Induced by the Energy Alignment of Charge Transfer and Local Triplet Excited States, *Adv. Opt. Mater.*, 2016, **4**, 597–607.
13 S. Reineke, F. Lindner, G. Schwartz, N. Seidler, K. Walzer, B. Lüssem and K. Leo, White Organic Light-Emitting Diodes With Fluorescent Tube Efficiency, *Nature*, 2009, **459**, 234–238.
14 Y. Tao, K. Yuan, T. Chen, P. Xu, H. Li, R. Chen, C. Zheng, L. Zhang and W. Huang, Thermally Activated Delayed Fluorescence Materials Towards the Breakthrough of Organoelectronics, *Adv. Mater.*, 2014, **26**, 7931–7958.
15 E. Spuling, N. Sharma, I. D. W. Samuel, E. Zysman-Colman and S. Bräse, (Deep) Blue Through-Space Conjugated TADF Emitters Based on [2.2]Paracyclophanes, *Chem. Commun.*, 2018, **54**, 9278–9281.
16 T. Hatakeyama, K. Shiren, K. Nakajima, S. Nomura, S. Nakatsuka, K. Kinoshita, J. Ni, Y. Ono and T. Ikuta, Ultrapure Blue Thermally Activated Delayed Fluorescence Molecules: Efficient HOMO–LUMO Separation by the Multiple Resonance Effect, *Adv. Mater.*, 2016, **28**, 2777–2781.
17 M. Auffray, D. H. Kim, J. U. Kim, F. Bencheikh, D. Kreher, Q. Zhang, A. D'Aléo, J.-C. Ribierre, F. Mathevet and C. Adachi, Dithia[3.3]paracyclophane Core: A Versatile Platform for Triplet State Fine-Tuning and Through-Space TADF Emission, *Chem. – Asian J.*, 2019, **14**, 1921–1925.
18 J. Lee, N. Aizawa and T. Yasuda, Molecular Engineering of Phosphacycle-Based Thermally Activated Delayed Fluorescence Materials for Deep-Blue OLEDs, *J. Mater. Chem. C*, 2018, **6**, 3578–3583.
19 X. Liang, Z.-P. Yan, H.-B. Han, Z.-G. Wu, Y.-X. Zheng, H. Meng, J.-L. Zuo and W. Huang, Peripheral Amplification of Multi-Resonance Induced Thermally Activated Delayed Fluorescence for Highly Efficient OLEDs, *Angew. Chem., Int. Ed.*, 2018, **57**, 11316–11320.
20 Y. J. Cho, S. K. Jeon, S.-S. Lee, E. Yu and J. Y. Lee, Donor Interlocked Molecular Design for Fluorescence-like Narrow Emission in Deep Blue Thermally Activated Delayed Fluorescent Emitters, *Chem. Mater.*, 2016, **28**, 5400–5405.
21 L. Mei, J. Hu, X. Cao, F. Wang, C. Zheng, Y. Tao, X. Zhang and W. Huang, The Inductive-Effect of Electron Withdrawing Trifluoromethyl for Thermally Activated Delayed Fluorescence: Tunable Emission from Tetra- to Penta-Carbazole in Solution Processed Blue OLEDs, *Chem. Commun.*, 2015, **51**, 13024–13027.
22 H. Wang, L. Xie, Q. Peng, L. Meng, Y. Wang, Y. Yi and P. Wang, Novel Thermally Activated Delayed Fluorescence Materials–Thioxanthone Derivatives and Their Applications for Highly Efficient OLEDs, *Adv. Mater.*, 2014, **26**, 5198–5204.
23 R. Furue, T. Nishimoto, I. S. Park, J. Lee and T. Yasuda, Aggregation-Induced Delayed Fluorescence Based on Donor/Acceptor-Tethered Janus Carborane Triads: Unique Photophysical Properties of Nondoped OLEDs, *Angew. Chem., Int. Ed.*, 2016, **55**, 7171–7175.
24 H. F. Higginbotham, P. Pander, R. Rybakiewicz, M. K. Etherington, S. Maniam, M. Zagorska, A. Pron, A. P. Monkman and P. Data, Triphenylamine Disubstituted Naphthalene Diimide: Elucidation of Excited States Involved in TADF and Application in Near-Infrared Organic Light Emitting Diodes, *J. Mater. Chem. C*, 2018, **6**, 8219–8225.
25 G. Xie, X. Li, D. Chen, Z. Wang, X. Cai, D. Chen, Y. Li, K. Liu, Y. Cao and S.-J. Su, Evaporation- and Solution-Process-Feasible Highly Efficient Thianthrene-9,9′,10,10′-Tetraoxide-Based Thermally Activated Delayed Fluorescence Emitters with Reduced Efficiency Roll-Off, *Adv. Mater.*, 2016, **28**, 181–187.
26 T.-A. Lin, T. Chatterjee, W.-L. Tsai, W.-K. Lee, M.-J. Wu, M. Jiao, K.-C. Pan, C.-L. Yi, C.-L. Chung, K.-T. Wong and C.-C. Wu, Sky-Blue Organic Light Emitting Diode with 37% External Quantum Efficiency Using Thermally Activated Delayed Fluorescence from Spiroacridine-Triazine Hybrid, *Adv. Mater.*, 2016, **28**, 6976–6983.
27 T. Takahashi, K. Shizu, T. Yasuda, K. Togashi and C. Adachi, Donor–Acceptor-Structured 1,4-Diazatriphenylene Derivatives Exhibiting Thermally Activated Delayed Fluorescence: Design and Synthesis, Photophysical Properties and OLED Characteristics, *Sci. Technol. Adv. Mater.*, 2014, **15**, 034202.

28 H. Tanaka, K. Shizu, H. Nakanotani and C. Adachi, Twisted Intramolecular Charge Transfer State for Long-Wavelength Thermally Activated Delayed Fluorescence, *Chem. Mater.*, 2013, **25**, 3766–3771.

29 J. Lee, K. Shizu, H. Tanaka, H. Nomura, T. Yasuda and C. Adachi, Oxadiazole- and Triazole-Based Highly-Efficient Thermally Activated Delayed Fluorescence Emitters for Organic Light-Emitting Diodes, *J. Mater. Chem. C*, 2013, **1**, 4599–4604.

30 C. Duan, J. Li, C. Han, D. Ding, H. Yang, Y. Wei and H. Xu, Multi-dipolar Chromophores Featuring Phosphine Oxide as Joint Acceptor: A New Strategy toward High-Efficiency Blue Thermally Activated Delayed Fluorescence Dyes, *Chem. Mater.*, 2016, **28**, 5667–5679.

31 D.-Y. Chen, W. Liu, C.-J. Zheng, K. Wang, F. Li, S. L. Tao, X.-M. Ou and X.-H. Zhang, Isomeric Thermally Activated Delayed Fluorescence Emitters for Color Purity-Improved Emission in Organic Light-Emitting Devices, *ACS Appl. Mater. Interfaces*, 2016, **8**, 16791–16798.

32 N. Aizawa, C.-J. Tsou, I. S. Park and T. Yasuda, Aggregation-Induced Delayed Fluorescence From Phenothiazine-Containing Donor–Acceptor Molecules for High-Efficiency Non-Doped Organic Light-Emitting Diodes, *Polym. J.*, 2017, **49**, 197–202.

33 S. Xu, T. Liu, Y. Mu, Y.-F. Wang, Z. Chi, C.-C. Lo, S. Liu, Y. Zhang, A. Lien and J. Xu, An Organic Molecule with Asymmetric Structure Exhibiting Aggregation-Induced Emission, Delayed Fluorescence, and Mechanoluminescence, *Angew. Chem., Int. Ed.*, 2015, **54**, 874–878.

34 D. R. Lee, B. S. Kim, C. W. Lee, Y. Im, K. S. Yook, S.-H. Hwang and J. Y. Lee, Above 30% External Quantum Efficiency in Green Delayed Fluorescent Organic Light-Emitting Diodes, *ACS Appl. Mater. Interfaces*, 2015, **7**, 9625–9629.

35 S. K. Jeon and J. Y. Lee, Highly Efficient Exciplex Organic Light-Emitting Diodes by Exciplex Dispersion in the Thermally Activated Delayed Fluorescence Host, *Org. Electron.*, 2020, **76**, 105477.

36 B. Wex and B. R. Kaafarani, Perspective on Carbazole-Based Organic Compounds as Emitters and Hosts in TADF Applications, *J. Mater. Chem. C*, 2017, **5**, 8622–8653.

37 Y. J. Cho, K. S. Yook and J. Y. Lee, High Efficiency in a Solution-Processed Thermally Activated Delayed-Fluorescence Device Using a Delayed-Fluorescence Emitting Material with Improved Solubility, *Adv. Mater.*, 2014, **26**, 6642–6646.

38 S. Wu, M. Aonuma, Q. Zhang, S. Huang, T. Nakagawa, K. Kuwabara and C. Adachi, High-Efficiency Deep-Blue Organic Light-Emitting Diodes Based on a Thermally Activated Delayed Fluorescence Emitter, *J. Mater. Chem. C*, 2014, **2**, 421–424.

39 G. H. Kim, R. Lampande, M. J. Park, H. W. Bae, J. H. Kong, J. H. Kwon, J. H. Park, Y. W. Park and C. E. Song, Highly Efficient Bipolar Host Materials with Indenocarbazole and Pyrimidine Moieties for Phosphorescent Green Light-Emitting Diodes, *J. Phys. Chem. C*, 2014, **118**, 28757–28763.

40 D. R. Lee, J. M. Choi, C. W. Lee and J. Y. Lee, Ideal Molecular Design of Blue Thermally Activated Delayed Fluorescent Emitter for High Efficiency, Small Singlet–Triplet Energy Splitting, Low Efficiency Roll-Off, and Long Lifetime, *ACS Appl. Mater. Interfaces*, 2016, **8**, 23190–23196.

41 K. Sun, Y. Sun, T. Huang, J. Luo, W. Jiang and Y. Sun, Design Strategy of Yellow Thermally Activated Delayed Fluorescent Dendrimers and Their Highly Efficient Non-Doped Solution-Processed OLEDs with Low Driving Voltage, *Org. Electron.*, 2017, **42**, 123–130.

42 K. Albrecht, K. Matsuoka, K. Fujita and K. Yamamoto, Carbazole Dendrimers as Solution-Processable Thermally Activated Delayed-Fluorescence Materials, *Angew. Chem., Int. Ed.*, 2015, **54**, 5677–5682.

43 D. R. Lee, S.-H. Hwang, S. K. Jeon, C. W. Lee and J. Y. Lee, Benzofurocarbazole and Benzothienocarbazole as Donors for Improved Quantum Efficiency in Blue Thermally Activated Delayed Fluorescent Devices, *Chem. Commun.*, 2015, **51**, 8105–8107.

44 N. Sharma, E. Spuling, C. M. Mattern, W. Li, O. Fuhr, Y. Tsuchiya, C. Adachi, S. Bräse, I. D. W. Samuel and E. Zysman-Colman, Turn on of Sky-Blue Thermally Activated Delayed Fluorescence and Circularly Polarized Luminescence (CPL) via Increased Torsion by a Bulky Carbazolophane Donor, *Chem. Sci.*, 2019, **10**, 6689–6696.

45 B. Huang, W. Jiang, Y. Y. Liu, Y. A. Zhang, Y. P. Yang, Y. Dai, X. X. Ban, H. G. Xu and Y. M. Sun, Thermally Activated Delayed Fluorescence Materials Based on Carbazole/Sulfone, *Adv. Mater. Res.*, 2014, **1044–1045**, 158–163.

46 Y. Im and J. Y. Lee, Effect of the Position of Nitrogen in Pyridoindole on Photophysical Properties and Device Performances of α-, β-, γ-Carboline Based High Triplet Energy Host Materials for deep Blue Devices, *Chem. Commun.*, 2013, **49**, 5948–5950.

47 J.-W. Jun, K.-M. Lee, O. Y. Kim, J. Y. Lee and S.-H. Hwang, Synthesis of a Dibenzothiophene/Carboline/Carbazole Hybrid Bipolar Host Material for Green Phosphorescent OLEDs, *Synth. Met.*, 2016, **213**, 7–11.

48 S. Y. Byeon, S. K. Jeon, S.-H. Hwang and J. Y. Lee, Carbazole-Carboline Core as a Backbone Structure of High Triplet Energy Host Materials, *Dyes Pigm.*, 2015, **120**, 258–264.

49 Z. Zhang, J. Xie, Z. Wang, B. Shen, H. Wang, M. Li, J. Zhang and J. Cao, Manipulation of Electron Deficiency of δ-Carboline Derivatives as Bipolar Hosts for Blue Phosphorescent Organic Light-Emitting Diodes with High Efficiency at 1000 cd m^{-2}, *J. Mater. Chem. C*, 2016, **4**, 4226–4235.

50 C. W. Lee and J. Y. Lee, Above 30% External Quantum Efficiency in Blue Phosphorescent Organic Light-Emitting Diodes Using Pyrido[2,3-*b*]indole Derivatives as Host Materials, *Adv. Mater.*, 2013, **25**, 5450–5454.

51 C.-C. Lai, M.-J. Huang, H.-H. Chou, C.-Y. Liao, P. Rajamalli and C.-H. Cheng, m-Indolocarbazole Derivative as a Universal Host Material for RGB and White Phosphorescent OLEDs, *Adv. Funct. Mater.*, 2015, **25**, 5548–5556.

52 K. S. Yook and J. Y. Lee, Bipolar Host Materials for Organic Light-Emitting Diodes, *Chem. Rec.*, 2016, **16**, 159–172.
53 M.-S. Lin, L.-C. Chi, H.-W. Chang, Y.-H. Huang, K.-C. Tien, C.-C. Chen, C.-H. Chang, C.-C. Wu, A. Chaskar, S.-H. Chou, H.-C. Ting, K.-T. Wong, Y.-H. Liu and Y. Chi, A Diarylborane-Substituted Carbazole as a Universal Bipolar Host Material for Highly Efficient Electrophosphorescence Devices, *J. Mater. Chem.*, 2012, **22**, 870–876.
54 M.-S. Lin, S.-J. Yang, H.-W. Chang, Y.-H. Huang, Y.-T. Tsai, C.-C. Wu, S.-H. Chou, E. Mondal and K.-T. Wong, Incorporation of a CN Group into mCP: A New Bipolar Host Material for Highly Efficient Blue and White Electrophosphorescent Devices, *J. Mater. Chem.*, 2012, **22**, 16114–16120.
55 C. S. Oh, J. M. Choi and J. Y. Lee, Chemical Bond Stabilization and Exciton Management by CN Modified Host Material for Improved Efficiency and Lifetime in Blue Phosphorescent Organic Light-Emitting Diodes, *Adv. Opt. Mater.*, 2016, **4**, 1281–1287.
56 Q. Zhang, J. Li, K. Shizu, S. Huang, S. Hirata, H. Miyazaki and C. Adachi, Design of Efficient Thermally Activated Delayed Fluorescence Materials for Pure Blue Organic Light Emitting Diodes, *J. Am. Chem. Soc.*, 2012, **134**, 14706–14709.
57 S. Hirata, Y. Sakai, K. Masui, H. Tanaka, S. Y. Lee, H. Nomura, N. Nakamura, M. Yasumatsu, H. Nakanotani, Q. Zhang, K. Shizu, H. Miyazaki and C. Adachi, Highly Efficient Blue Electroluminescence Based on Thermally Activated Delayed Fluorescence, *Nat. Mater.*, 2015, **14**, 330–336.
58 M. Colella, A. Danos and A. P. Monkman, Less Is More: Dilution Enhances Optical and Electrical Performance of a TADF Exciplex, *J. Phys. Chem. Lett.*, 2019, **10**, 793–798.
59 K. Masui, H. Nakanotani and C. Adachi, Analysis of Exciton Annihilation in High-Efficiency Sky-Blue Organic Light-Emitting Diodes With Thermally Activated Delayed Fluorescence, *Org. Electron.*, 2013, **14**, 2721–2726.
60 W. J. Hehre, R. Ditchfield and J. A. Pople, Self—Consistent Molecular Orbital Methods. XII. Further Extensions of Gaussian—Type Basis Sets for Use in Molecular Orbital Studies of Organic Molecules, *J. Chem. Phys.*, 1972, **56**, 2257–2261.
61 J. R. Adsetts, R. Zhang, L. Yang, K. Chu, J. M. Wong, D. A. Love and Z. Ding, Efficient White Electrochemiluminescent Emission From Carbon Quantum Dot Films, *Front. Chem.*, 2020, **8**, 580022.
62 K. Chu, J. R. Adsetts, S. He, Z. Zhan, L. Yang, J. M. Wong, D. A. Love and Z. Ding, Electrogenerated Chemiluminescence and Electroluminescence of N-Doped Graphene Quantum Dots Fabricated from an Electrochemical Exfoliation Process in Nitrogen-Containing Electrolytes, *Chem. – Eur. J.*, 2020, **26**, 15892–15900.
63 J. R. Adsetts, S. Hoesterey, C. Gao, D. A. Love and Z. Ding, Electrochemiluminescence and Photoluminescence of Carbon Quantum Dots Controlled by Aggregation-Induced Emission, Aggregation-Caused Quenching and Interfacial Reactions, *Langmuir*, 2020, **36**, 14432–14442.
64 K. Chu, J. R. Adsetts, C. Moore and Z. Ding, Spooling Electroluminescence Spectroscopy of $Ru(bpy)_3^{2+}$ Light-Emitting Electrochemical Cells with an Atomic Layer Deposited Zinc Oxide Electron-Transporting/Hole-Blocking Interlayer, *ACS Appl. Electron. Mater.*, 2020, **2**, 3825–3830.
65 E. W. Grabner and E. Brauer, Electrochemiluminescence of Energy-Deficient Systems II. The Role of Excimer Formation in the Pure Perylene System, *Ber. Bunsen-Ges. Phys. Chem.*, 1971, **76**, 111–114.
66 L. Yang, B. Zhang, L. Fu, K. Fu and G. Zou, Efficient and Monochromatic Electrochemiluminescence of Aqueous-Soluble Au Nanoclusters via Host-Guest Recognition, *Angew. Chem., Int. Ed.*, 2019, **58**, 6901–6905.
67 R. Ishimatsu, S. Matsunami, T. Kasahara, J. Mizuno, T. Edura, C. Adachi, K. Nakano and T. Imato, Electrogenerated Chemiluminescence of Donor-Acceptor Molecules with Thermally Activated Delayed Fluorescence, *Angew. Chem., Int. Ed.*, 2014, **53**, 6993–6996.
68 S. W. Feldberg, A Possible Method for Distinguishing between Triplet–Triplet Annihilation and Direct Singlet Formation in Electrogenerated Chemiluminescence, *J. Phys. Chem.*, 1966, **70**, 3928–3930.
69 L. Yang, D. Koo, J. Wu, J. M. Wong, T. Day, R. Zhang, H. Kolongoda, K. Liu, J. Wang, Z. Ding and B. L. Pagenkopf, Benzosiloles with Crystallization-Induced Emission Enhancement of Electrochemiluminescence: Synthesis, Electrochemistry, and Crystallography, *Chemistry*, 2020, **26**, 11715–11721.
70 J. R. Adsetts and Z. Ding, Film Electrochemiluminescence Controlled by Interfacial Reactions Along with Aggregation-, Matrix-Coordination-, and Crystallization-Induced Emissions, *ChemPlusChem*, 2021, **86**, 155–165.
71 J. M. Wong, R. Zhang, P. Xie, L. Yang, M. Zhang, R. Zhou, R. Wang, Y. Shen, B. Yang, H. B. Wang and Z. Ding, Revealing Crystallization-Induced Blue-Shift Emission of a Di-Boron Complex by Enhanced Photoluminescence and Electrochemiluminescence, *Angew. Chem., Int. Ed.*, 2020, **59**, 17461–17466.
72 D. Ege, W. G. Becker and A. J. Bard, Electrogenerated Chemiluminescent Determination of $Ru(bpy)_3^{2+}$ at Low Levels, *Anal. Chem.*, 1984, **56**, 2413–2417.
73 E. A. Chandross and F. I. Sonntag, A Novel Chemiluminescent Electron-Transfer Reaction, *J. Am. Chem. Soc.*, 1964, **86**, 3179–3180.
74 D. M. Hercules, Chemiluminescence Resulting From Electrochemically Generated Species, *Science*, 1964, **145**, 808–809.
75 K. S. V. Santhanam and A. J. Bard, Chemiluminescence of Electrogenerated 9,10-Diphenylathracene Anion Radical, *J. Am. Chem. Soc.*, 1965, **87**, 139–140.
76 Z. Liu, W. Qi and G. Xu, Recent Advances in Electrochemiluminescence, *Chem. Soc. Rev.*, 2015, **44**, 3117–3142.
77 M. K. Etherington, J. Gibson, H. F. Higginbotham, T. J. Penfold and A. P. Monkman, Revealing the Spin–Vibronic Coupling Mechanism of Thermally Activated Delayed Fluorescence, *Nat. Commun.*, 2016, **7**, 13680.

78 Z. Zeng, P. Huang, Y. Kong, L. Tong, B. Zhang, Y. Luo, L. Chen, Y. Zhang, D. Han and L. Niu, Nanoencapsulation Strategy: Enabling Electrochemiluminescence of Thermally Activated Delayed Fluorescence (TADF) Emitters in Aqueous Media, *Chem. Commun.*, 2021, **57**, 5262–5265.

79 R. Ishimatsu, T. Edura, C. Adachi, K. Nakano and T. Imato, Photophysical Properties and Efficient, Stable, Electrogenerated Chemiluminescence of Donor–Acceptor Molecules Exhibiting Thermal Spin Upconversion, *Chem. – Eur. J.*, 2016, **22**, 4889–4898.

80 A. Kapturkiewicz, Electrochemical Generation of Excited Intramolecular Charge-Transfer States, *ChemElectroChem*, 2017, **4**, 1604–1638.

81 M. Y. Wong, G. J. Hedley, G. Xie, L. S. Kölln, I. D. W. Samuel, A. Pertegás, H. J. Bolink and E. Zysman-Colman, Light-Emitting Electrochemical Cells and Solution-Processed Organic Light-Emitting Diodes Using Small Molecule Organic Thermally Activated Delayed Fluorescence Emitters, *Chem. Mater.*, 2015, **27**, 6535–6542.

82 J. N. Demas and G. A. Crosby, The Measurement of Photoluminescence Quantum Yields. A Review, *J. Phys. Chem.*, 1971, **75**, 991–1024.

83 W. H. Melhuish, QUANTUM EFFICIENCIES OF FLUORESCENCE OF ORGANIC SUBSTANCES: EFFECT OF SOLVENT AND CONCENTRATION OF THE FLUORESCENT SOLUTE1, *J. Phys. Chem.*, 1961, **65**, 229–235.

84 J. Adsetts, R. Zhang, L. Yang, K. Chu, J. Wong, D. A. Love and Z. Ding, Efficient White Electrochemiluminescent Emission from Carbon Quantum Dot Films, *Front. Chem.*, 2020, **8**, 865–878.

85 L. R. Faulkner, H. Tachikawa and A. J. Bard, Electrogenerated Chemiluminescence. VII. The Influence of an External Magnetic Field on Luminescence Intensity, *J. Am. Chem. Soc.*, 1972, **94**, 691–699.

86 M. Y. Wong, S. Krotkus, G. Copley, W. Li, C. Murawski, D. Hall, G. J. Hedley, M. Jaricot, D. B. Cordes, A. M. Z. Slawin, Y. Olivier, D. Beljonne, L. Muccioli, M. Moral, J.-C. Sancho-Garcia, M. C. Gather, I. D. W. Samuel and E. Zysman-Colman, Deep-Blue Oxadiazole-Containing Thermally Activated Delayed Fluorescence Emitters for Organic Light-Emitting Diodes, *ACS Appl. Mater. Interfaces*, 2018, **10**, 33360–33372.

87 W. H. Melhuish, Quantum Efficiencies of Fluorescence of Organic Substances: Effect of Solvent and Concentration of the Fluorescent Solute, *J. Phys. Chem.*, 1961, **65**, 229–235.

88 N. G. Connelly and W. E. Geiger, Chemical Redox Agents for Organometallic Chemistry, *Chem. Rev.*, 1996, **96**, 877–910.

89 C. M. Cardona, W. Li, A. E. Kaifer, D. Stockdale and G. C. Bazan, Electrochemical Considerations for Determining Absolute Frontier Orbital Energy Levels of Conjugated Polymers for Solar Cell Applications, *Adv. Mater.*, 2011, **23**, 2367–2371.

90 M. Moral, L. Muccioli, W. J. Son, Y. Olivier and J. C. Sancho-García, Theoretical Rationalization of the Singlet–Triplet Gap in OLEDs Materials: Impact of Charge-Transfer Character, *J. Chem. Theory Comput.*, 2015, **11**, 168–177.

91 C. Adamo and V. Barone, Toward Reliable Density Functional Methods Without Adjustable Parameters: The PBE0 Model, *J. Chem. Phys.*, 1999, **110**, 6158–6170.

92 R. Ditchfield, W. J. Hehre and J. A. Pople, Self-Consistent Molecular-Orbital Methods. IX. An Extended Gaussian-Type Basis for Molecular-Orbital Studies of Organic Molecules, *J. Chem. Phys.*, 1971, **54**, 724–728.

93 S. Hirata and M. Head-Gordon, Time-Dependent Density Functional Theory Within the Tamm–Dancoff Approximation, *Chem. Phys. Lett.*, 1999, **314**, 291–299.

94 Y. Geng, A. D'Aleo, K. Inada, L.-S. Cui, J. U. Kim, H. Nakanotani and C. Adachi, Donor–σ–Acceptor Motifs: Thermally Activated Delayed Fluorescence Emitters with Dual Upconversion, *Angew. Chem., Int. Ed.*, 2017, **56**, 16536–16540.

95 M. J. Frisch, G. W. Trucks, H. B. Schlegel, G. E. Scuseria, M. A. Robb, J. R. Cheeseman, J. A. Montgomery, T. Vreven, K. N. Kudin, J. C. Burant, J. M. Millam, S. S. Iyengar, J. Tomasi, V. Barone, B. Mennucci, M. Cossi, G. Scalmani, N. Rega, G. A. Petersson, H. Nakatsuji, M. Hada, M. Ehara, K. Toyota, R. Fukuda, J. Hasegawa, M. Ishida, T. Nakajima, Y. Honda, O. Kitao, H. Nakai, M. Klene, X. Li, J. E. Knox, H. P. Hratchian, J. B. Cross, V. Bakken, C. Adamo, J. Jaramillo, R. Gomperts, R. E. Stratmann, O. Yazyev, A. J. Austin, R. Cammi, C. Pomelli, J. W. Ochterski, P. Y. Ayala, K. Morokuma, G. A. Voth, P. Salvador, J. J. Dannenberg, V. G. Zakrzewski, S. Dapprich, A. D. Daniels, M. C. Strain, O. Farkas, D. K. Malick, A. D. Rabuck, K. Raghavachari, J. B. Foresman, J. V. Ortiz, Q. Cui, A. G. Baboul, S. Clifford, J. Cioslowski, B. B. Stefanov, G. Liu, A. Liashenko, P. Piskorz, I. Komaromi, R. L. Martin, D. J. Fox, T. Keith, A. Laham, C. Y. Peng, A. Nanayakkara, M. Challacombe, P. M. W. Gill, B. Johnson, W. Chen, M. W. Wong, C. Gonzalez and J. A. Pople, *Gaussian 03, Revision C.02*.

96 H. Noda, X.-K. Chen, H. Nakanotani, T. Hosokai, M. Miyajima, N. Notsuka, Y. Kashima, J.-L. Brédas and C. Adachi, Critical Role of Intermediate Electronic States for Spin-Flip Processes in Charge-Transfer-Type Organic Molecules with Multiple Donors and Acceptors, *Nat. Mater.*, 2019, **18**, 1084–1090.

97 O. V. Klymenko, I. Svir and C. Amatore, A New Approach for the Simulation of Electrochemiluminescence (ECL), *ChemPhysChem*, 2013, **14**, 2237–2250.

98 E. A. Chandross and F. I. Sonntag, Chemiluminescent Electron-Transfer Reactions of Radical Anions, *J. Am. Chem. Soc.*, 1966, **88**, 1089–1096.

99 R. Coehoorn, P. A. Bobbert and H. van Eersel, Förster-Type Triplet-Polaron Quenching in Disordered Organic Semiconductors, *Phys. Rev. B*, 2017, **96**, 184203.

100 N. E. Tokel-Takvoryan, R. E. Hemingway and A. J. Bard, Electrogenerated Chemiluminescence. XIII. Electrochemical and Electrogenerated Chemiluminescence Studies of Ruthenium Chelates, *J. Am. Chem. Soc.*, 1973, **95**, 6582–6589.

101 N. E. Tokel and A. J. Bard, Electrogenerated Chemiluminescence. IX. Electrochemistry and emission From Systems Containing Tris(2,2'-bipyridine)ruthenium(II) Dichloride, *J. Am. Chem. Soc.*, 1972, **94**, 2862–2863.

102 W. L. Wallace and A. J. Bard, Electrogenerated Chemiluminescence. 35. Temperature Dependence of the ECL Efficiency of $Ru(bpy)_3^{2+}$ in Acetonitrile and Evidence for Very High Excited State Yields from Electron Transfer Reactions, *J. Phys. Chem.*, 1979, **83**, 1350–1357.

103 F. E. Lytle and D. M. Hercules, Chemiluminescence From The Reduction of Aromatic Amine Cations and Ruthenium(III) Chelates, *Photochem. Photobiol.*, 1970, **13**, 123–133.

104 H. Saiki, K. Takami and T. Tominaga, Diffusion of Porphyrins and Quinones in Organic Solvents, *Phys. Chem. Chem. Phys.*, 1998, **1**, 303–306.

105 G. J. Barbante, C. F. Hogan, D. J. Wilson, N. A. Lewcenko, F. M. Pfeffer, N. W. Barnett and P. S. Francis, Simultaneous Control of Spectroscopic and Electrochemical Properties in Functionalised Electrochemiluminescent Tris(2,2'-bipyridine)-ruthenium(II) Complexes, *Analyst*, 2011, **136**, 1329–1338.

106 C. A. Parker and C. G. Hatchard, Delayed Fluorescence From Solutions of Anthracene and Phenanthrene, *Proc. R. Soc. London, Ser. A*, 1962, **269**, 574–584.

107 J. Grüne, N. Bunzmann, M. Meinecke, V. Dyakonov and A. Sperlich, Kinetic Modeling of Transient Electroluminescence Reveals TTA as an Efficiency-Limiting Process in Exciplex-Based TADF OLEDs, *J. Phys. Chem. C*, 2020, **124**, 25667–25674.

108 A. Niwa, S. Haseyama, T. Kobayashi, T. Nagase, K. Goushi, C. Adachi and H. Naito, Triplet-Triplet Annihilation in a Thermally Activated Delayed Fluorescence Emitter Lightly Doped in a Host, *Appl. Phys. Lett.*, 2018, **113**, 083301–083305.

109 K. Masui, H. Nakanotani and C. Adachi, Analysis of Exciton Annihilation in High-Efficiency Sky Blue Organic Light-Emitting Diodes with Thermally Activated Delayed Fluorescence, *Org. Electron.*, 2013, **14**, 2721–2726.

110 W. Miao, Electrogenerated Chemiluminescence and Its Biorelated Applications, *Chem. Rev.*, 2008, **108**, 2506–2553.

111 M. J. Cormier, D. M. Hercules and J. Lee, *Chemiluminescence and Bioluminescence*, Springer, Boston MA, 1973.

112 J. Rosenmund and K. Doblhofer, The Effects of Uncompensated Solution Resistance and Rate of the Homogenous Electron Transfer Reaction on Electrochemiluminescence Transients, *J. Electroanal. Chem.*, 1995, **396**, 77–83.

113 R. Kabe and C. Adachi, Organic Long Persistent Luminescence, *Nature*, 2017, **550**, 384–387.

114 S. Tan, K. Jinnai, R. Kabe and C. Adachi, Long-Persistent Luminescence From an Exciplex-Based Organic Light-Emitting Diode, *Adv. Mater.*, 2021, e2008844.

115 K. Jinnai, N. Nishimura, C. Adachi and R. Kabe, Thermally Activated Processes in an Organic Long-Persistent Luminescence System, *Nanoscale*, 2021, **13**, 8412–8417.

116 W. Li, Z. Li, C. Si, M. Y. Wong, K. Jinnai, A. K. Gupta, R. Kabe, C. Adachi, W. Huang, E. Zysman-Colman and I. D. W. Samuel, Organic Long-Persistent Luminescence from a Thermally Activated Delayed Fluorescence Compound, *Adv. Mater.*, 2020, **32**, e2003911.

117 J. Cornil, D. A. dos Santos, X. Crispin, R. Silbey and J. L. Bredas, Influence of Interchain Interactions on the Absorption and Luminescence of Conjugated Oligomers and Polymers: A Quantum-Chemical Characterization, *J. Am. Chem. Soc.*, 1998, **120**, 1289–1299.

118 P. Tourneur, F. Lucas, C. Quinton, Y. Olivier, R. Lazzaroni, P. Viville, J. Cornil and C. Poriel, White-Light Electroluminescence From a Layer Incorporating a Single Fully-Organic Spiro Compound with Phosphine Oxide Substituents, *J. Mater. Chem. C*, 2020, **8**, 14462–14468.

119 R. Newcomb, J. S. Bangsund, K. W. Hershey, D. C. K. Rathwell, H. Y. Na, J. H. Jeon, P. Trefonas and R. J. Holmes, Role of Host Excimer Formation in the Degradation of Organic Light-Emitting Devices, *Appl. Phys. Lett.*, 2020, **116**, 063302–0633028.

120 T. T. Bui, F. Goubard, M. Ibrahim-Ouali, D. Gigmes and F. Dumur, Thermally Activated Delayed Fluorescence Emitters for Deep Blue Organic Light Emitting Diodes: A Review of Recent Advances, *Appl. Sci.*, 2018, **8**, 494–517.